Electronic Supplementary Material

Hybrid multifunctionalized mesostructured stellate silica nanoparticles loaded with Tb^{3+}/Eu^{3+} β-diketonate complexes as efficient ratiometric emissive thermometers working in water

Tristan Pelluau,[a] Saad Sene,[a] Lamiaa M.A. Ali,[b,c] Gautier Félix,[a] Faustine Manhes,[b] Albano N. Carneiro Neto,[d] Luís D. Carlos,[d] Belen Albela,[e] Laurent Bonneviot,[e] Erwan Oliviero,[a] Magali Gary-Bobo,[b] Yannick Guari*[a] and Joulia Larionova*[a]

[a]*ICGM, Univ. Montpellier, CNRS, ENSCM, Montpellier, France. E-mail : joulia.larionova@umontpellier.fr, yannick.guari@umontpellier.fr*

[b]*IBMM, Univ. Montpellier, CNRS, ENSCM, Montpellier, France.*

[c]*Department of Biochemistry, Medical Research Institute, University of Alexandria, Alexandria, Egypt.*

[d]*Department of Physics and CICECO – Aveiro Institute of Materials, University of Aveiro, 3810-193, Aveiro, Portugal. E-mail:* lcarlos@ua.pt

[e]*Laboratoire de Chimie, ENS de Lyon, Université de Lyon, Lyon, France.*

Contents

1. Tables and Figures

Table S1. Comparison of thermometric performance for some illustrative examples of nanothermometers based on nanoparticles containing lanthanide complexes or organic dyes working in water. tta= 2-thenoyltrifluoroacetone, btfa = 4,4,4-trifluoro-1-phenyl-2,4-butanedione; bpeta = 1,2–bis(4–pyridyl)ethane); tppo = triphenylphosphine oxide; L1 = 4,4,4-trifluoro-1-phenyl-1,3-butadionate, L2 = 4,4,4-trifluoro-1-(4-chlorophenyl)-1,3-butadionate, PMO = Periodic Mesoporous Organosilica

	Nanoparticles' size (nm)	Sensor's specificity	Temperature range	Maximal thermal sensitivity, S_r (%K^{-1})	Ref.
Core@shell Bi_2SiO_2:Yb^{3+}-Er^{3+}@SiO_2	~190 nm	Upconverting nanoparticles, emission in the NIR region	293 - 343 K	1.1 (300 K)	64
$NaGdF_4Yb^{3+}$:Er^{3+}@SiO_2/Eu(tta)$_3$	~40 nm	Self-referenced, dual mode sensor, emission in the NIR region	293 – 330 K	2.3 (329 K)	38
Fe_2O_3@SiO_2/[Tb(btfa)MeOH(bpeta)]/ /[Eu(btfa)MeOH(bpeta)]	Not well definite shape, ~100 - 400	Dispersible in water, but the measurements have been done in polymer films	10 – 350 K	4.9 (120 – 190 K)	32
Multicore beads of Fe_2O_3@polymer shell (P4VP-b-P(PMEGA-co-PEGA)/[Tb(btfa)$_3$(H_2O)$_2$]/ /[Eu(btfa)$_3$(H_2O)$_2$]	~50 nm	Self-referencing, excitation at 365 nm, emission in the visible region	295 – 315 K	5.8 (296 K)	39
Core@shell SiO_2@PMAA/[Tb/EuL$_1$tppo] or [Tb/SmL$_2$tppo]	~150 – 500	Self-referenced, measurements in water, Toxicity investigations excitation at UV, emission in the visible region	278 – 323 K	3.8 (293 K for Tb^{3+}/Eu^{3+}) 3.3 (293 K for Tb^{3+}/Sm^{3+})	37
Bipyrimidine-functionalized PMO grafted with Dy(acac)$_3$, Tb/Eu(acac)$_3$ or Tb/Sm(acac)$_3$	Irregular shape, 100 – 400 nm	Self-referenced, excitation at UV, emission in the visible region	278 – 323 K	2.7 (278 K for Tb^{3+}/Sm^{3+}) 1.9 (260 K for Tb^{3+}/Eu^{3+})	35
Pyridine dicarboxoamide/1,10-phenantroline functionalized PMO with coordinated Eu^{3+}/Tb^{3+} or Sm^{3+}/Tb^{3+} ions	50 – 70 nm	Self-referenced λ_{ex} = 326 nm, emission in the visible region	260 – 460 K	1.6 (360 K for Tb^{3+}/Eu^{3+}) 2.4 (340 K)	36
Mesoporous SiO_2 nanoparticles encapsulated Rhodamine 6G/Rhodamine B dyes	50 nm	FRET between the dyes, λ_{ex} = 488 nm, emission in the visible region	278 – 323 K	1.0 (293 – 323 K)	40
Tb^{3+}/Eu^{3+} ions coordinated to pyromellitic acid functionalized nanodiamond	Irregular shape, 60 – 140 nm	λ_{ex} = 254 nm, emission in visible region	50 – 300 K	0.5 (275 K)	65
Fe_3O_4@SiO_2@pNIPAM-co-RhBITC/Au containing Rodamin B and isothiocyanate dyes	150 nm	Thermometry in living cells, emission in the visible region	299 – 314 K	-4.84	66
Stellate SiO_2/[(Tb/Eu)$_9$(acac)$_{16}$(μ_3-OH)$_8$(μ_4-O)(μ_4-OH)]·H_2O	95.0	Thermometry in water	293 – 343 K	1.4 (315 K)	This work
		Thermometry in PBS	293 – 343 K	4.1 (343 K)	
		Thermometry in cells	293 – 313 K	8.6 (313 K)	
	92.3	Thermometry in water	293 – 343 K	2.3 (329 K)	

Table S2. Integrated areas of the Eu^{3+} $^5D_0 \rightarrow {}^7F_2$ ($^{S_{0\rightarrow2}}$) and Eu^{3+} $^5D_0 \rightarrow {}^7F_4$ ($^{S_{0\rightarrow4}}$) transitions with the $^{S_{0\rightarrow1}}$ set to 1. Values of $^{\Omega_\lambda}$ (λ = 2, 4, and 6), in units of 10^{-20} cm^2, for Ln^{3+} in compounds **1**, **MSN-1**, and **MSN-2**. The values in parentheses are the forced electric dipole (FED) contributions obtained from the JOYSpectra program.[9]

Sample	Ion*	$S_{0\rightarrow2}$	$S_{0\rightarrow4}$	Ω_2	Ω_4	$\Omega_{6\dagger}$
1	**Eu^{3+}**	11.8	3.1	20.0 (0.90)	10.8 (1.14)	3.4 (1.77)
	Tb^{3+}	–	–	14.8 (0.16)	5.7 (0.17)	1.0 (0.26)
MSN-1	**Eu^{3+}**	2.3	1.7	4.0 (0.07)	5.9 (0.11)	1.9 (0.24)
	Tb^{3+}	–	–	3.5 (0.05)	4.4 (0.06)	1.2 (0.12)
MSN-2	**Eu^{3+}**	2.2	1.7	3.7 (0.03)	5.8 (0.11)	1.8 (0.21)
	Tb^{3+}	–	–	3.2 (0.02)	4.4 (0.06)	1.1 (0.10)

† Theoretically obtained; * Tb^{3+} intensity parameters were obtained theoretically using the same environment parameters obtained from the Eu^{3+} analogue.

Table S3. Tb^{3+} to Eu^{3+} (forward) energy transfer pathways for R = 3.44 Å in both **MSN-1** and **MSN-2** at 300 K.

Path.	From	To	δ	W_{d-d}	W_{d-q}	W_{q-q}	W_{ex}	W_{md-md}	W^f
1	$^5D_4 \rightarrow {}^7F_4$	$^7F_1 \rightarrow {}^5D_1$	−1663	7.9×10^{-12}	4.3×10^{-8}	5.9×10^{-5}	9.4	0	9.4
2	$^5D_4 \rightarrow {}^7F_2$	$^7F_1 \rightarrow {}^5D_0$	−1596	0	0	0	3.0×10^{1}	0	3.0×10^{1}
3	$^5D_3 \rightarrow {}^7F_4$	$^7F_0 \rightarrow {}^5D_3$	−1434	0	0	0	9.1×10^{2}	0	9.1×10^{2}
4	$^5D_3 \rightarrow {}^7F_4$	$^7F_1 \rightarrow {}^5D_3$	−1199	1.6×10^{-8}	1.0×10^{-4}	6.1×10^{-1}	1.5×10^{4}	0	1.5×10^{4}
5	$^5D_4 \rightarrow {}^7F_3$	$^7F_0 \rightarrow {}^5D_0$	−1143	3.6×10^{-10}	3.0×10^{-6}	4.3×10^{-2}	6.6×10^{4}	0	6.6×10^{4}
6	$^5D_3 \rightarrow {}^7F_5$	$^7F_0 \rightarrow {}^5L_6$	−1137	9.3×10^{-5}	3.6×10^{-2}	0	7.1×10^{4}	0	7.1×10^{4}
7	$^5D_4 \rightarrow {}^7F_6$	$^7F_0 \rightarrow {}^5D_2$	−1039	1.7×10^{-7}	1.1×10^{-3}	7.0	2.6×10^{5}	0	2.6×10^{5}
8	$^5D_4 \rightarrow {}^7F_3$	$^7F_1 \rightarrow {}^5D_0$	−908	0	0	0	6.2×10^{5}	1.1×10^{-3}	6.2×10^{5}
9	$^5D_3 \rightarrow {}^7F_0$	$^7F_0 \rightarrow {}^5D_2$	−907	0	0	0	1.3×10^{6}	0	1.3×10^{6}
10	$^5D_3 \rightarrow {}^7F_5$	$^7F_1 \rightarrow {}^5L_6$	−902	1.1×10^{-5}	4.3×10^{-3}	0	6.7×10^{5}	0	6.7×10^{5}
11	$^5D_4 \rightarrow {}^7F_6$	$^7F_1 \rightarrow {}^5D_2$	−804	5.5×10^{-8}	3.5×10^{-4}	2.3	2.0×10^{6}	0	2.0×10^{6}
12	$^5D_3 \rightarrow {}^7F_1$	$^7F_0 \rightarrow {}^5D_2$	−684	6.6×10^{-6}	5.1×10^{-2}	6.4×10^{2}	1.5×10^{7}	0	1.5×10^{7}
13	$^5D_3 \rightarrow {}^7F_0$	$^7F_1 \rightarrow {}^5D_2$	−672	0	0	0	8.1×10^{6}	0	8.1×10^{6}
14	$^5D_4 \rightarrow {}^7F_5$	$^7F_0 \rightarrow {}^5D_1$	−631	0	0	0	2.5×10^{7}	1.2×10^{-3}	2.5×10^{7}
15	$^5D_3 \rightarrow {}^7F_1$	$^7F_1 \rightarrow {}^5D_2$	−449	1.1×10^{-6}	8.8×10^{-3}	1.1×10^{2}	6.2×10^{7}	0	6.2×10^{7}
16	$^5D_3 \rightarrow {}^7F_2$	$^7F_0 \rightarrow {}^5D_2$	−229	5.0×10^{-4}	3.5	3.6×10^{4}	6.6×10^{8}	0	6.6×10^{8}
17	$^5D_3 \rightarrow {}^7F_5$	$^7F_0 \rightarrow {}^5D_3$	−167	1.3×10^{-5}	7.0×10^{-2}	1.9×10^{2}	9.7×10^{8}	0	9.7×10^{8}
18	$^5D_4 \rightarrow {}^7F_4$	$^7F_0 \rightarrow {}^5D_0$	−164	0	0	0	9.9×10^{8}	0	9.9×10^{8}
19	$^5D_3 \rightarrow {}^7F_6$	$^7F_0 \rightarrow {}^5G_2$	−156	4.7×10^{-4}	2.5	0	1.0×10^{9}	0	1.0×10^{9}
20	$^5D_3 \rightarrow {}^7F_6$	$^7F_0 \rightarrow {}^5L_7$	−121	0	0	0	1.3×10^{9}	0	1.3×10^{9}
21	$^5D_3 \rightarrow {}^7F_2$	$^7F_1 \rightarrow {}^5D_2$	6	3.6×10^{-5}	2.6×10^{-1}	2.6×10^{3}	1.2×10^{9}	1.9×10^{-2}	1.2×10^{9}
22	$^5D_4 \rightarrow {}^7F_5$	$^7F_1 \rightarrow {}^5D_1$	15	3.3×10^{-3}	3.0×10^{1}	5.1×10^{5}	1.2×10^{9}	3.6×10^{-3}	1.2×10^{9}
23	$^5D_3 \rightarrow {}^7F_5$	$^7F_1 \rightarrow {}^5D_3$	68	1.4×10^{-3}	1.8	3.7×10^{3}	1.1×10^{9}	0	1.1×10^{9}
24	$^5D_4 \rightarrow {}^7F_4$	$^7F_1 \rightarrow {}^5D_0$	71	0	0	0	1.1×10^{9}	1.8×10^{-1}	1.1×10^{9}
25	$^5D_3 \rightarrow {}^7F_6$	$^7F_1 \rightarrow {}^5G_2$	79	1.7×10^{-4}	8.9×10^{-1}	0	1.1×10^{9}	0	1.1×10^{9}
26	$^5D_3 \rightarrow {}^7F_6$	$^7F_1 \rightarrow {}^5L_7$	114	1.7×10^{-2}	0	0	1.1×10^{9}	0	1.1×10^{9}
27	$^5D_3 \rightarrow {}^7F_3$	$^7F_0 \rightarrow {}^5D_2$	459	3.2×10^{-4}	2.4	2.9×10^{4}	1.1×10^{9}	0	1.1×10^{9}
28	$^5D_3 \rightarrow {}^7F_3$	$^7F_1 \rightarrow {}^5D_2$	694	2.2×10^{-6}	1.7×10^{-2}	2.0×10^{2}	1.8×10^{8}	0	1.8×10^{8}
29	$^5D_3 \rightarrow {}^7F_6$	$^7F_0 \rightarrow {}^5L_6$	911	6.1×10^{-2}	0	0	9.9×10^{7}	0	9.9×10^{7}
30	$^5D_4 \rightarrow {}^7F_5$	$^7F_0 \rightarrow {}^5D_0$	1103	6.1×10^{-7}	5.6×10^{-3}	9.5×10^{1}	2.2×10^{7}	0	2.2×10^{7}
31	$^5D_3 \rightarrow {}^7F_6$	$^7F_1 \rightarrow {}^5L_6$	1146	5.7×10^{-5}	0	0	7.4×10^{6}	0	7.4×10^{6}
32	$^5D_4 \rightarrow {}^7F_5$	$^7F_1 \rightarrow {}^5D_0$	1338	0	0	0	1.2×10^{6}	0	1.2×10^{6}
33	$^5D_4 \rightarrow {}^7F_6$	$^7F_0 \rightarrow {}^5D_1$	1417	0	0	0	1.1×10^{6}	0	1.1×10^{6}
34	$^5D_3 \rightarrow {}^7F_4$	$^7F_0 \rightarrow {}^5D_2$	1438	1.0×10^{-6}	1.1×10^{-2}	2.1×10^{2}	8.4×10^{5}	0	8.4×10^{5}
35	$^5D_3 \rightarrow {}^7F_0$	$^7F_0 \rightarrow {}^5D_1$	1549	0	0	0	2.3×10^{5}	0	2.3×10^{5}
36	$^5D_4 \rightarrow {}^7F_6$	$^7F_1 \rightarrow {}^5D_1$	1652	2.1×10^{-8}	1.3×10^{-4}	8.9×10^{-1}	3.2×10^{4}	0	3.2×10^{4}
37	$^5D_3 \rightarrow {}^7F_4$	$^7F_1 \rightarrow {}^5D_2$	1673	1.2×10^{-9}	1.3×10^{-5}	2.5×10^{-1}	2.4×10^{4}	0	2.4×10^{4}
38	$^5D_3 \rightarrow {}^7F_1$	$^7F_0 \rightarrow {}^5D_1$	1772	0	0	0	1.4×10^{4}	0	1.4×10^{4}
39	$^5D_3 \rightarrow {}^7F_0$	$^7F_1 \rightarrow {}^5D_1$	1784	0	0	0	5.5×10^{3}	0	5.5×10^{3}
40	$^5D_3 \rightarrow {}^7F_6$	$^7F_0 \rightarrow {}^5D_3$	1881	0	0	0	2.9×10^{3}	0	2.9×10^{3}
41	$^5D_3 \rightarrow {}^7F_1$	$^7F_1 \rightarrow {}^5D_1$	2007	9.8×10^{-11}	7.6×10^{-7}	9.4×10^{-3}	2.1×10^{2}	0	2.1×10^{2}
42	$^5D_3 \rightarrow {}^7F_6$	$^7F_1 \rightarrow {}^5D_3$	2116	2.2×10^{-11}	2.0×10^{-8}	0	3.8×10^{1}	0	3.8×10^{1}
43	$^5D_3 \rightarrow {}^7F_2$	$^7F_0 \rightarrow {}^5D_1$	2227	0	0	0	1.2×10^{1}	0	1.2×10^{1}
44	$^5D_3 \rightarrow {}^7F_2$	$^7F_1 \rightarrow {}^5D_1$	2462	6.6×10^{-14}	4.7×10^{-10}	4.8×10^{-6}	8.4×10^{-2}	0	8.4×10^{-2}
45	$^5D_3 \rightarrow {}^7F_5$	$^7F_0 \rightarrow {}^5D_2$	2705	1.8×10^{-15}	1.0×10^{-11}	2.7×10^{-8}	1.4×10^{-3}	0	1.4×10^{-3}
46	$^5D_3 \rightarrow {}^7F_3$	$^7F_0 \rightarrow {}^5D_1$	2915	0	0	0	1.5×10^{-5}	0	1.5×10^{-5}
$W_{total}^{f} = \sum W^f =$				**1.3×10^{10}**					

Table S4. Eu^{3+} to Tb^{3+} (backward) energy transfer pathways for R = 3.44 Å in both **MSN-1** and **MSN-2** at 300 K.

Path.	From	To	δ	W_{d-d}	W_{d-q}	W_{q-q}	W_{ex}	W_{md-md}	W^b
1	$^5D_0 \rightarrow {}^7F_6$	$^7F_6 \rightarrow {}^5D_3$	−13850	0	0	0	0	0	0
2	$^5D_0 \rightarrow {}^7F_5$	$^7F_6 \rightarrow {}^5D_3$	−12792	0	0	0	1.6×10^{-291}	0	1.6×10^{-291}
3	$^5D_0 \rightarrow {}^7F_6$	$^7F_5 \rightarrow {}^5D_3$	−11802	7.1×10^{-262}	1.8×10^{-259}	0	1.1×10^{-249}	0	1.1×10^{-249}
4	$^5D_0 \rightarrow {}^7F_4$	$^7F_6 \rightarrow {}^5D_3$	−11766	4.8×10^{-259}	0	0	3.0×10^{-247}	0	3.0×10^{-247}
5	$^5D_0 \rightarrow {}^7F_5$	$^7F_5 \rightarrow {}^5D_3$	−10744	0	0	0	1.3×10^{-207}	0	1.3×10^{-207}
6	$^5D_0 \rightarrow {}^7F_3$	$^7F_6 \rightarrow {}^5D_3$	−10609	0	0	0	1.5×10^{-201}	0	1.5×10^{-201}
7	$^5D_0 \rightarrow {}^7F_2$	$^7F_6 \rightarrow {}^5D_3$	−9969	6.4×10^{-190}	3.8×10^{-186}	0	3.5×10^{-178}	0	3.5×10^{-178}
8	$^5D_0 \rightarrow {}^7F_4$	$^7F_5 \rightarrow {}^5D_3$	−9718	9.0×10^{-182}	2.3×10^{-179}	0	2.4×10^{-170}	0	2.4×10^{-170}
9	$^5D_0 \rightarrow {}^7F_1$	$^7F_6 \rightarrow {}^5D_3$	−9178	0	0	0	3.3×10^{-151}	0	3.3×10^{-151}
10	$^5D_0 \rightarrow {}^7F_0$	$^7F_6 \rightarrow {}^5D_3$	−8943	0	0	0	1.3×10^{-143}	0	1.3×10^{-143}
11	$^5D_0 \rightarrow {}^7F_3$	$^7F_5 \rightarrow {}^5D_3$	−8561	0	0	0	1.4×10^{-132}	0	1.4×10^{-132}
12	$^5D_0 \rightarrow {}^7F_6$	$^7F_6 \rightarrow {}^5D_4$	−8058	4.8×10^{-129}	3.5×10^{-126}	0	1.4×10^{-116}	0	1.4×10^{-116}
13	$^5D_0 \rightarrow {}^7F_2$	$^7F_5 \rightarrow {}^5D_3$	−7921	5.9×10^{-125}	3.6×10^{-121}	6.6×10^{-118}	1.3×10^{-113}	0	1.3×10^{-113}
14	$^5D_0 \rightarrow {}^7F_1$	$^7F_5 \rightarrow {}^5D_3$	−7130	0	0	0	4.8×10^{-92}	0	4.8×10^{-92}
15	$^5D_0 \rightarrow {}^7F_5$	$^7F_6 \rightarrow {}^5D_4$	−7000	0	0	0	9.6×10^{-88}	0	9.6×10^{-88}
16	$^5D_0 \rightarrow {}^7F_0$	$^7F_5 \rightarrow {}^5D_3$	−6895	0	0	0	4.8×10^{-86}	0	4.8×10^{-86}
17	$^5D_1 \rightarrow {}^7F_3$	$^7F_5 \rightarrow {}^5D_3$	−6827	6.8×10^{-96}	2.7×10^{-92}	4.7×10^{-89}	2.4×10^{-84}	0	2.4×10^{-84}
18	$^5D_1 \rightarrow {}^7F_6$	$^7F_6 \rightarrow {}^5D_4$	−6324	0	0	0	2.8×10^{-71}	0	2.8×10^{-71}
19	$^5D_1 \rightarrow {}^7F_2$	$^7F_5 \rightarrow {}^5D_3$	−6187	0	0	0	4.5×10^{-69}	0	4.5×10^{-69}
20	$^5D_0 \rightarrow {}^7F_6$	$^7F_5 \rightarrow {}^5D_4$	−6010	6.4×10^{-77}	2.0×10^{-73}	0	4.2×10^{-65}	0	4.2×10^{-65}
21	$^5D_0 \rightarrow {}^7F_4$	$^7F_6 \rightarrow {}^5D_4$	−5974	4.9×10^{-75}	3.5×10^{-72}	0	2.4×10^{-63}	0	2.4×10^{-63}
22	$^5D_1 \rightarrow {}^7F_1$	$^7F_5 \rightarrow {}^5D_3$	−5396	4.8×10^{-64}	2.9×10^{-60}	5.3×10^{-57}	4.2×10^{-52}	0	4.2×10^{-52}
23	$^5D_1 \rightarrow {}^7F_5$	$^7F_6 \rightarrow {}^5D_4$	−5266	0	0	0	1.5×10^{-48}	0	1.5×10^{-48}
24	$^5D_1 \rightarrow {}^7F_0$	$^7F_5 \rightarrow {}^5D_3$	−5161	0	0	0	1.8×10^{-47}	0	1.8×10^{-47}
25	$^5D_0 \rightarrow {}^7F_5$	$^7F_5 \rightarrow {}^5D_4$	−4952	0	0	0	1.7×10^{-43}	0	1.7×10^{-43}
26	$^5D_0 \rightarrow {}^7F_3$	$^7F_6 \rightarrow {}^5D_4$	−4817	0	0	0	4.7×10^{-40}	0	4.7×10^{-40}
27	$^5D_1 \rightarrow {}^7F_6$	$^7F_5 \rightarrow {}^5D_4$	−4276	0	0	0	1.2×10^{-31}	0	1.2×10^{-31}
28	$^5D_1 \rightarrow {}^7F_4$	$^7F_6 \rightarrow {}^5D_4$	−4240	3.4×10^{-42}	2.4×10^{-39}	0	4.1×10^{-30}	0	4.1×10^{-30}
29	$^5D_0 \rightarrow {}^7F_2$	$^7F_6 \rightarrow {}^5D_4$	−4177	1.0×10^{-40}	6.7×10^{-37}	3.2×10^{-33}	4.2×10^{-29}	0	4.2×10^{-29}
30	$^5D_0 \rightarrow {}^7F_4$	$^7F_5 \rightarrow {}^5D_4$	−3926	3.5×10^{-37}	1.1×10^{-33}	0	4.0×10^{-26}	0	4.0×10^{-26}
31	$^5D_0 \rightarrow {}^7F_1$	$^7F_6 \rightarrow {}^5D_4$	−3386	0	0	0	1.9×10^{-17}	0	1.9×10^{-17}
32	$^5D_1 \rightarrow {}^7F_5$	$^7F_5 \rightarrow {}^5D_4$	−3218	0	0	0	3.4×10^{-16}	0	3.4×10^{-16}
33	$^5D_0 \rightarrow {}^7F_0$	$^7F_6 \rightarrow {}^5D_4$	−3151	0	0	0	2.2×10^{-14}	0	2.2×10^{-14}
34	$^5D_1 \rightarrow {}^7F_3$	$^7F_6 \rightarrow {}^5D_4$	−3083	2.3×10^{-25}	1.0×10^{-21}	4.6×10^{-18}	1.5×10^{-13}	0	1.5×10^{-13}
35	$^5D_0 \rightarrow {}^7F_3$	$^7F_5 \rightarrow {}^5D_4$	−2769	0	0	0	9.2×10^{-11}	0	9.2×10^{-11}
36	$^5D_1 \rightarrow {}^7F_2$	$^7F_6 \rightarrow {}^5D_4$	−2443	0	0	0	2.7×10^{-6}	0	2.7×10^{-6}
37	$^5D_1 \rightarrow {}^7F_4$	$^7F_5 \rightarrow {}^5D_4$	−2192	3.2×10^{-16}	9.9×10^{-13}	0	8.9×10^{-5}	0	8.9×10^{-5}
38	$^5D_0 \rightarrow {}^7F_2$	$^7F_5 \rightarrow {}^5D_4$	−2129	3.5×10^{-15}	3.2×10^{-11}	4.8×10^{-7}	3.5×10^{-4}	0	3.5×10^{-4}
39	$^5D_1 \rightarrow {}^7F_1$	$^7F_6 \rightarrow {}^5D_4$	−1652	2.0×10^{-11}	1.3×10^{-7}	6.2×10^{-4}	3.2×10^{1}	0	3.2×10^{1}
40	$^5D_1 \rightarrow {}^7F_0$	$^7F_6 \rightarrow {}^5D_4$	−1417	0	0	0	1.6×10^{3}	0	1.6×10^{3}
41	$^5D_0 \rightarrow {}^7F_1$	$^7F_5 \rightarrow {}^5D_4$	−1338	0	0	0	5.9×10^{2}	9.9×10^{-8}	5.9×10^{2}
42	$^5D_0 \rightarrow {}^7F_0$	$^7F_5 \rightarrow {}^5D_4$	−1103	0	0	0	1.7×10^{4}	0	1.7×10^{4}
43	$^5D_1 \rightarrow {}^7F_3$	$^7F_5 \rightarrow {}^5D_4$	−1035	2.6×10^{-7}	1.8×10^{-3}	2.2×10^{1}	4.0×10^{4}	0	4.0×10^{4}
44	$^5D_1 \rightarrow {}^7F_2$	$^7F_5 \rightarrow {}^5D_4$	−395	0	0	0	2.9×10^{7}	1.7×10^{-1}	2.9×10^{7}
45	$^5D_1 \rightarrow {}^7F_1$	$^7F_5 \rightarrow {}^5D_4$	−15	8.7×10^{-4}	7.9	1.2×10^{5}	3.3×10^{8}	8.4×10^{-4}	3.3×10^{8}
46	$^5D_1 \rightarrow {}^7F_0$	$^7F_5 \rightarrow {}^5D_4$	631	0	0	0	7.7×10^{7}	5.9×10^{-3}	7.7×10^{7}
$W_{total}^{b} = \sum W^b =$							**4.4×10^{8}**		

Table S5. Tb–Eu distances (^{R}) and the occurrence coefficients ($^{O_i(x)}$ and $^{O_i(1-x)}$) with respect to the distances order (^{i}). ^{x} is the fraction of Eu^{3+} amount while $^{1-x}$ represents the Tb^{3+} amount.

		Tb–Eu distance order (i)					
		1	**2**	**3**	**4**	**5**	**11**
1 ($x = 0.05$)	R_i (Å)	3.62	3.65	3.73	3.74	5.11	9.92
	$O_i(x)$	0.83	0.87	0.82	0.83	0.39	0.79
	$O_i(1-x)$	0.09	0.08	0.08	0.10	0.04	0.04
2 ($x = 0.10$)	R_i (Å)	3.62	3.65	3.73	3.74	5.11	9.92
	$O_i(x)$	0.84	0.79	0.65	0.83	0.39	0.45
	$O_i(1-x)$	0.09	0.09	0.07	0.09	0.02	0.05
MSN-1 ($x = 0.05$)	R_i (Å)	3.44	3.44	3.52	3.55	5.06	9.92
	$O_i(x)$	0.83	0.87	0.82	0.83	0.39	0.79
	$O_i(1-x)$	0.09	0.08	0.08	0.10	0.04	0.04
MSN-2 ($x = 0.10$)	R_i (Å)	3.44	3.44	3.52	3.55	5.06	9.92
	$O_i(x)$	0.84	0.79	0.65	0.83	0.39	0.45
	$O_i(1-x)$	0.09	0.09	0.07	0.09	0.02	0.05

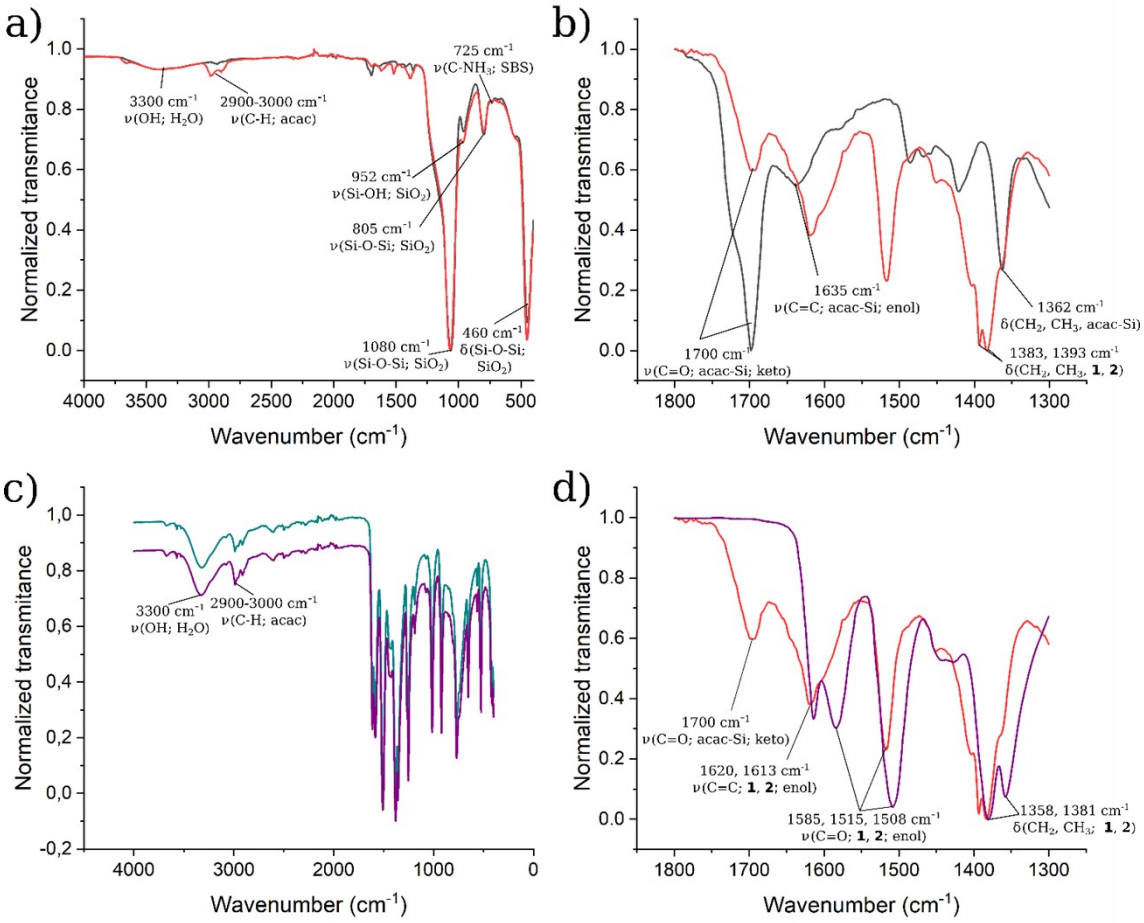

Figure S1. Infrared spectra of: a) **MSN** (black), **MSN-1** (red), b) **MSN** (black), **MSN-1** (red), in the 1800-1300 cm^{-1} window, c) compounds **1** (green) and **2** (purple), d) compared **MSN-2** (red) and **2** (purple) in the 1800-1300 cm^{-1} window.

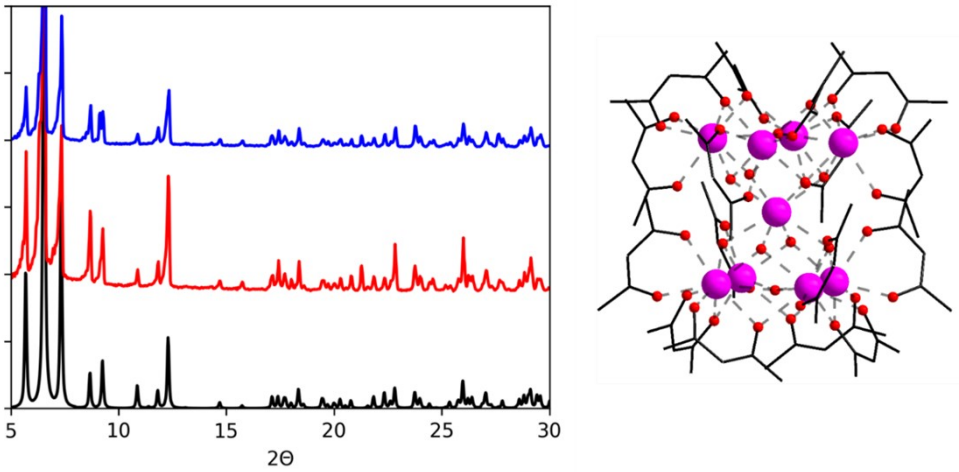

Figure S2. Powder XRD patterns of the referenced complex $[Tb_9(acac)_{16}(\mu_3\text{-}OH)_8(\mu_4\text{-}O)(\mu_4\text{-}OH)]\cdot H_2O$ (black) (S. Petit, F. Baril-Robert, G. Pilet, C. Reber and D. Luneau, *Dalton Trans.*, **2009**, 6809–6815) and complexes **1** (red) and **2** (blue).

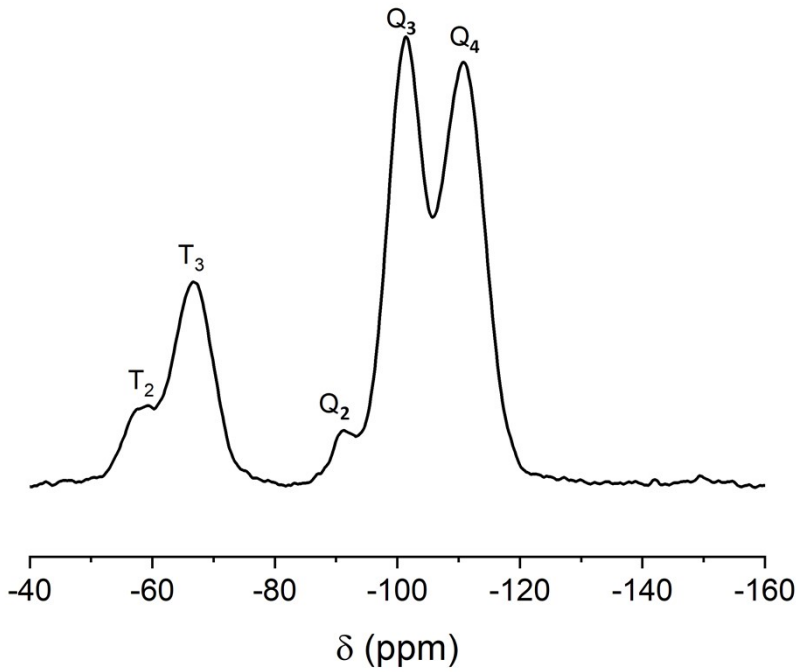

Figure S3. ^{29}Si CPMAS solid-state NMR of **MSN**.

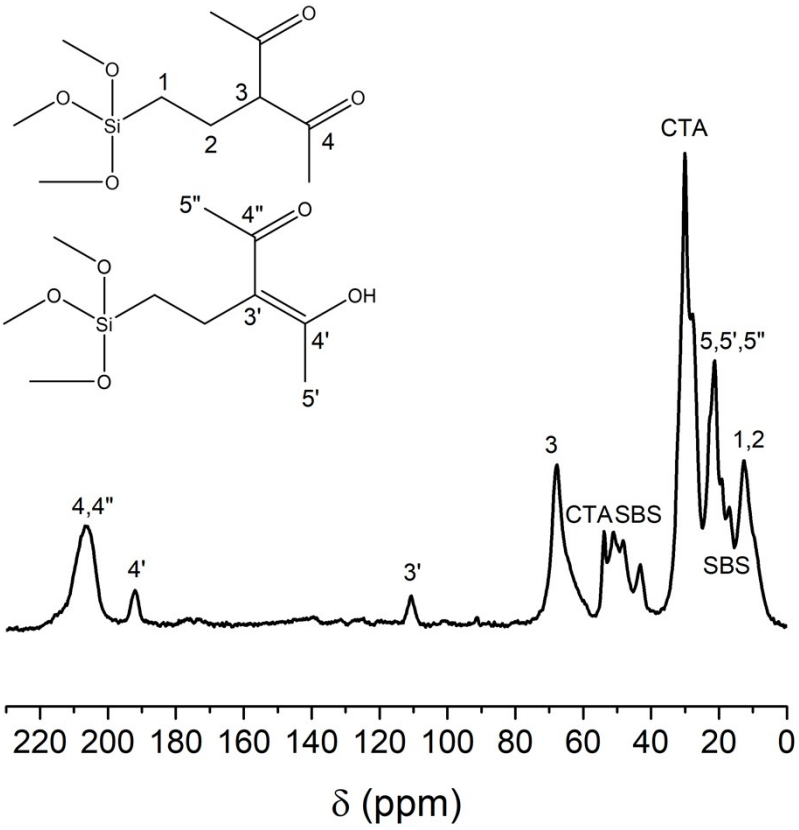

Figure S4. ^{13}C CPMAS solid-state NMR of **MSN**. CTA indicates the peaks from the remaining molecules of surfactant and SBS indicates the peaks of the zwitterion.

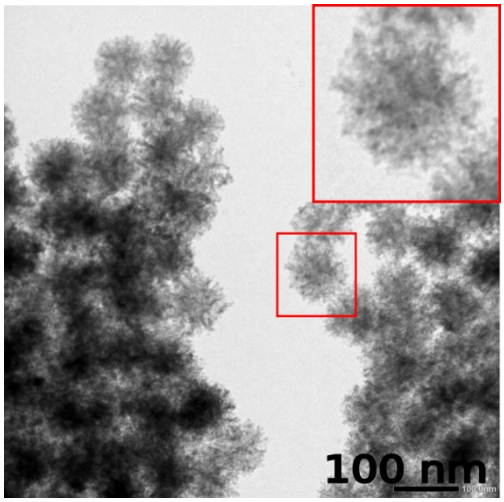

Figure S5. TEM image of functionalized hybrid silica **MSN-2**.

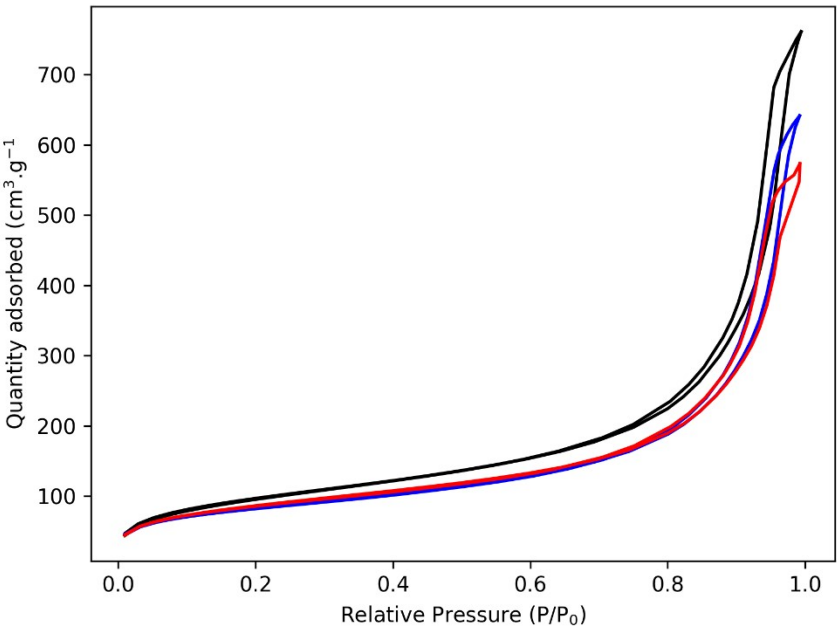

Figure S6. N_2 adsorption isotherms of: **MSN** (black), **MSN-1** (blue) and **MSN-2** (red).

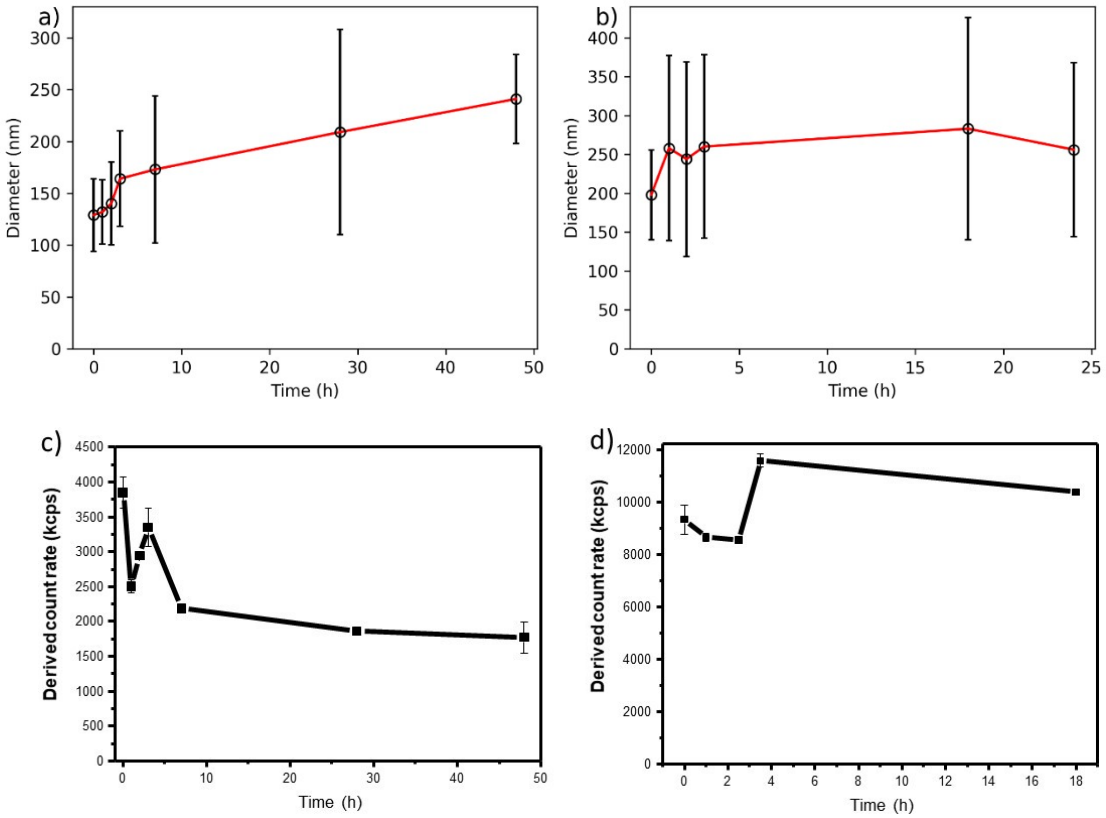

Figure S7. Size distributions for **MSN-1** averaged by intensity in water: (a) and in Fetal Bovine Serum (FBS) 10 %/90 % high glucose DMEM (b); Scattered light intensity for **MSN-1** in water (c) and in FBS 10%/90 % high glucose DMEM (d). The decrease in scattered intensity (c) observed within the first hours, followed by stabilization after approximately 10 hours, indicates a process of nanoparticle aggregation and settling in water. After 10 hours, the scattered light intensity remains relatively constant, indicating that the nanoparticles have reached a state of equilibrium. In the 10 % FBS/90% high glucose DMEM solution, a variation of only 20% in scattered light intensity was observed during the initial hours, followed by a relatively stable intensity thereafter.

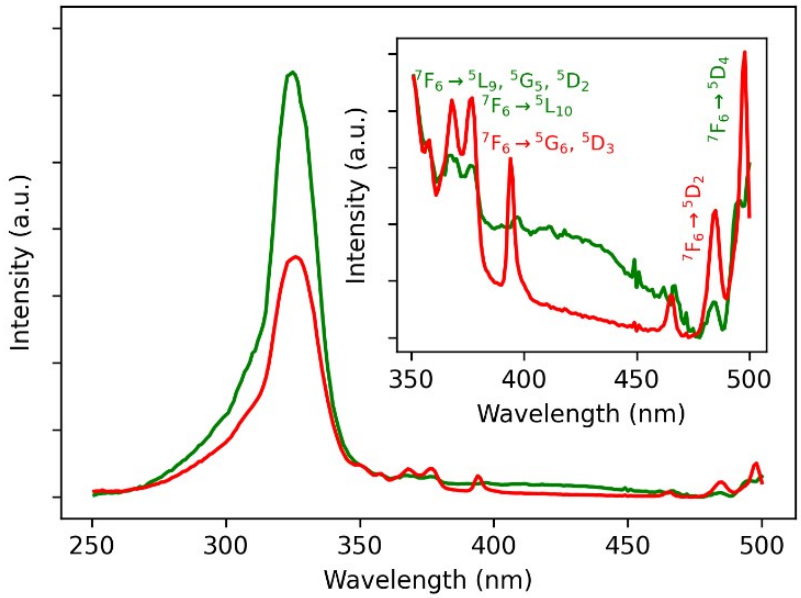

Figure S8. Excitation spectra of **MSN-1** monitored at λ_{em} = 545 nm (green) and 615 nm (red) measured at 77 K in solid state.

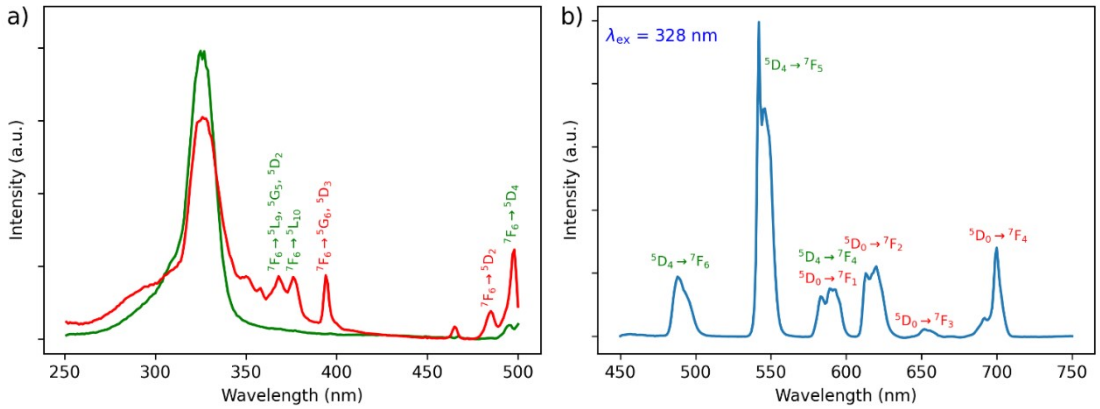

Figure S9. a) Excitation spectra of **MSN-2** monitored at λ_{em} = 545 nm (green) and 615 nm (red) measured at 77 K in solid state, and b) Emission spectra of **MSN-2** performed with λ_{ex} = 328 nm at 77 K and at room temperature in the solid state.

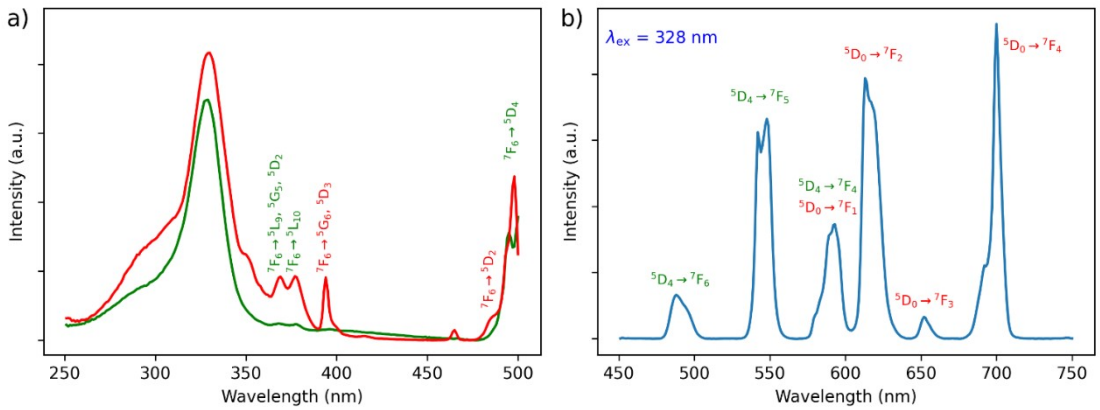

Figure S10. a) Excitation spectra of **MSN-2** monitored at λ_{em} = 545 (green) and 615 nm (red) measured at room temperature in solid state, and b) emission spectra of **MSN-2** performed with λ_{ex} = 328 nm at room temperature in the solid state.

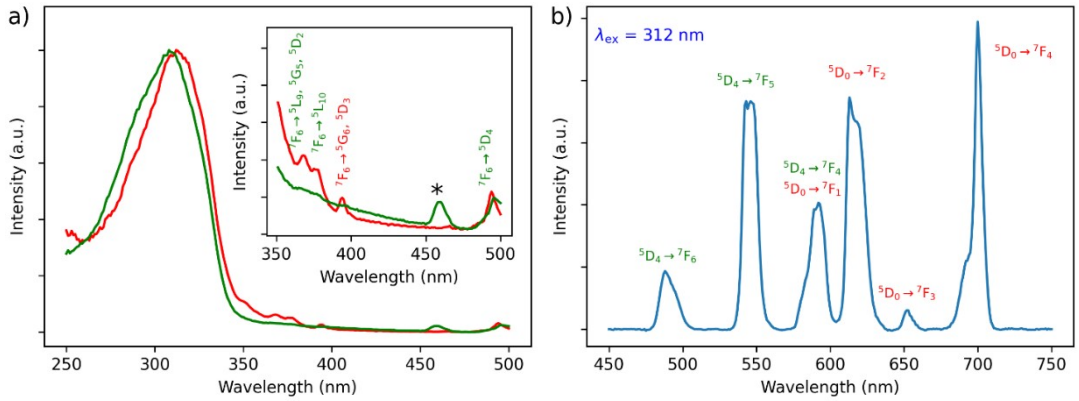

Figure S11. a) Excitation spectra of **MSN-1** monitored at λ_{em} = 545 (green) and 615 nm (red) measured at room temperature in water, and b) emission spectra of **MSN-1** performed with λ_{ex} = 312 nm at room temperature. * Raman scattering peak of water

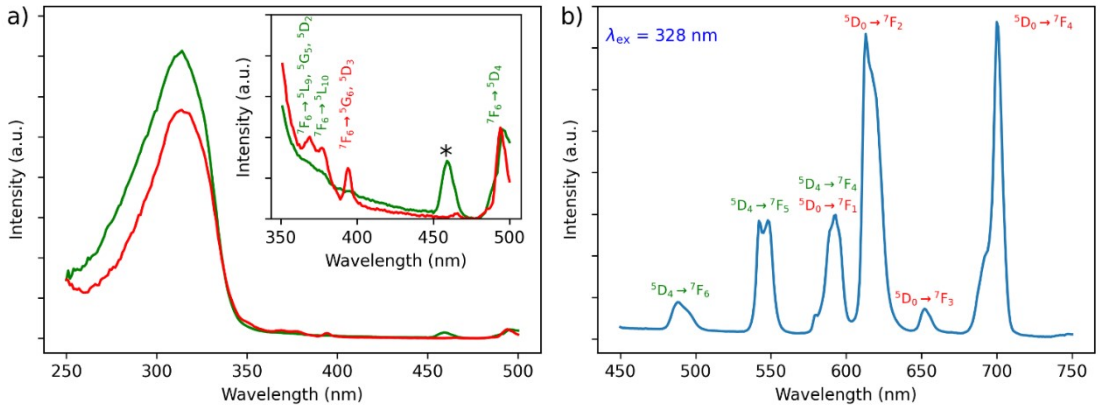

Figure S12. a) Excitation spectra of **MSN-2** monitored at λ_{em} = 545 (green) and 615 nm (red) measured at room temperature in water, and b) emission spectra of **MSN-2** performed with λ_{ex} = 312 nm at room temperature. * Raman scattering peak of water.

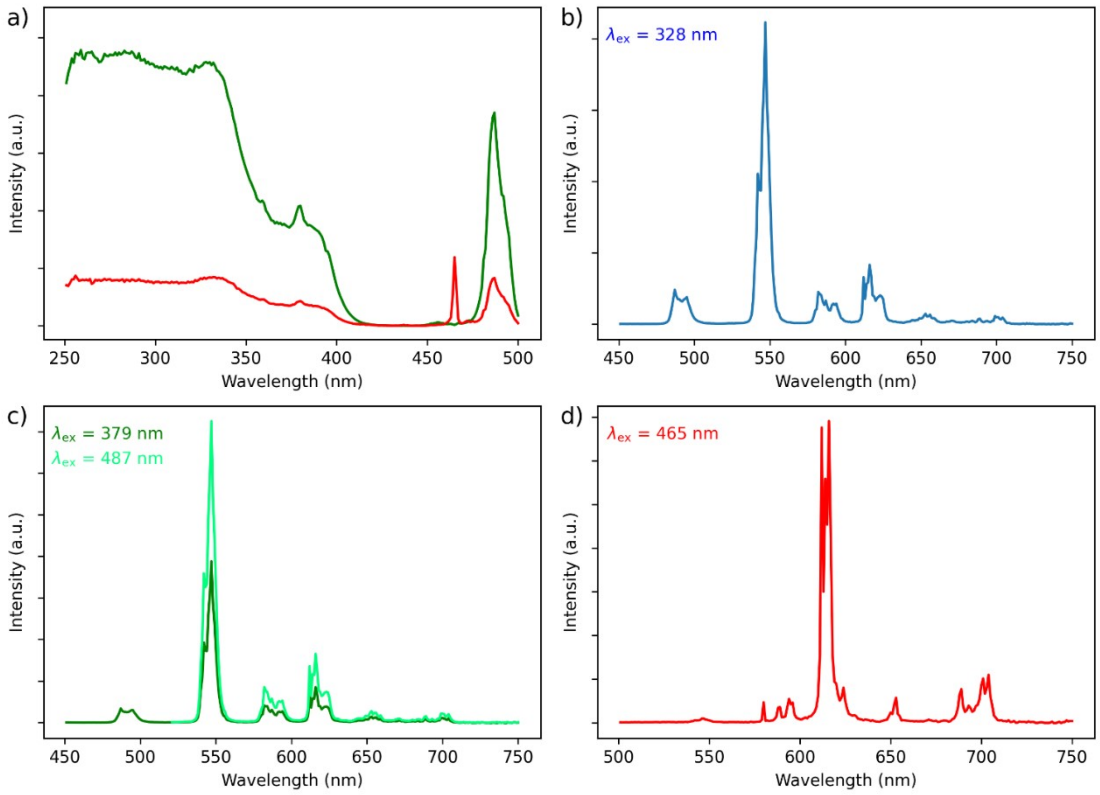

Figure S13. a) Excitation spectra of complex **1** monitored at λ_{em} = 545 (green) and 615 nm (red) measured at room temperature in solid state, b) Emission spectra of **1** performed with λ_{ex} = 328 nm at room temperature in solid state. c) Emission spectra of **1** performed with λ_{ex} = 379 and 487 nm at room temperature in solid state and d) emission spectra of **1** performed with λ_{ex} = 465 nm at room temperature in solid state.

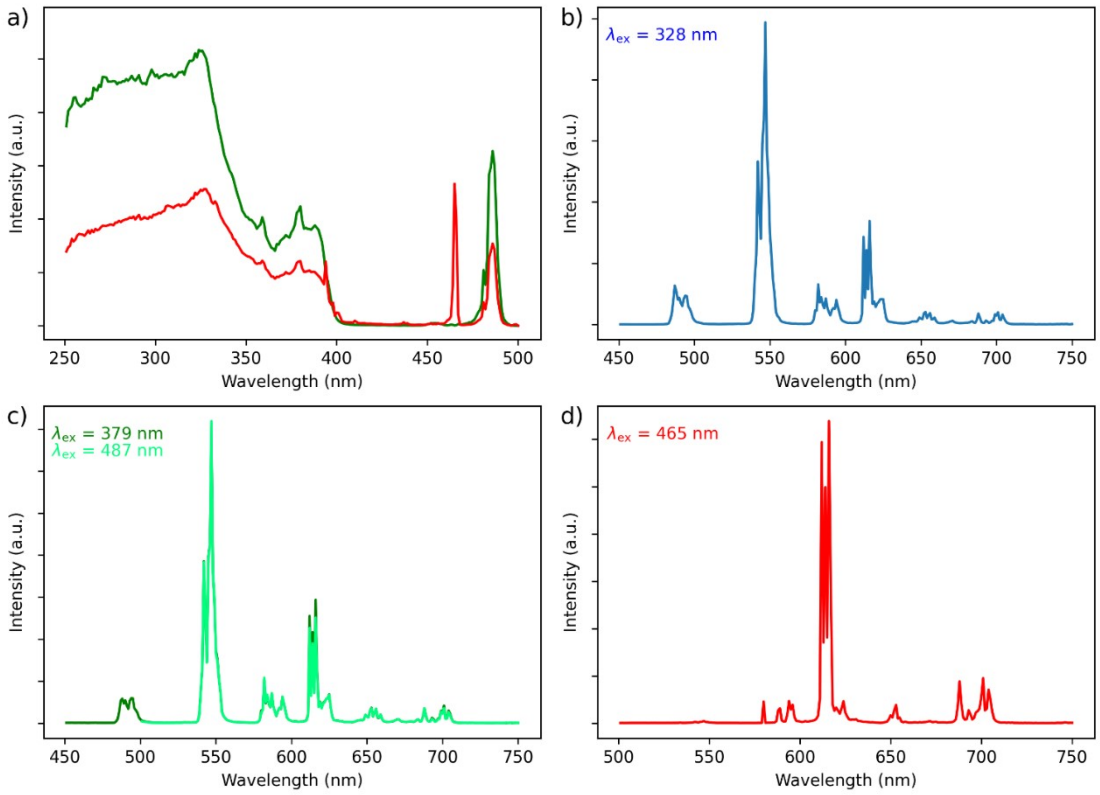

Figure S14. a) Excitation spectra of **1** monitored at λ_{em} = 545 (green) and 615 nm (red) measured at 77K in solid state, b) emission spectra of **1** performed with λ_{ex} = 328 nm at 77K in solid state, c) emission spectra of **1** performed with λ_{ex} = 379 and 487 nm at 77K in solid state and d) emission spectra of **1** performed with λ_{ex} = 465 nm at 77K in solid state.

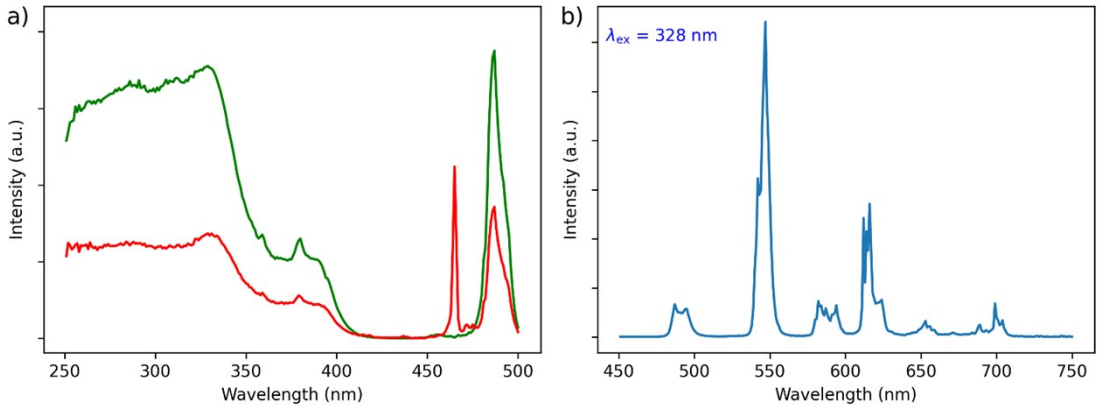

Figure S15. a) Excitation spectra of **2** monitored at λ_{em} = 545 (green) and 615 nm (red) measured at room temperature in solid state. b) Emission spectra of **2** performed with λ_{ex} = 328 nm at room temperature in solid state.

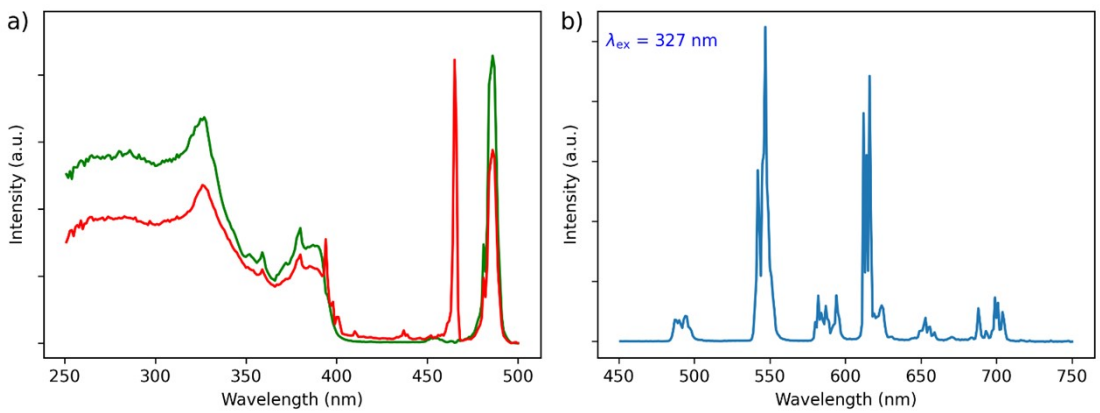

Figure S16. a) Excitation spectra of **2** monitored at λ_{em} = 545 (green) and 615 nm (red) measured at 77K in solid state, b) emission spectra of **2** performed with λ_{ex} = 328 nm at 77K in solid state.

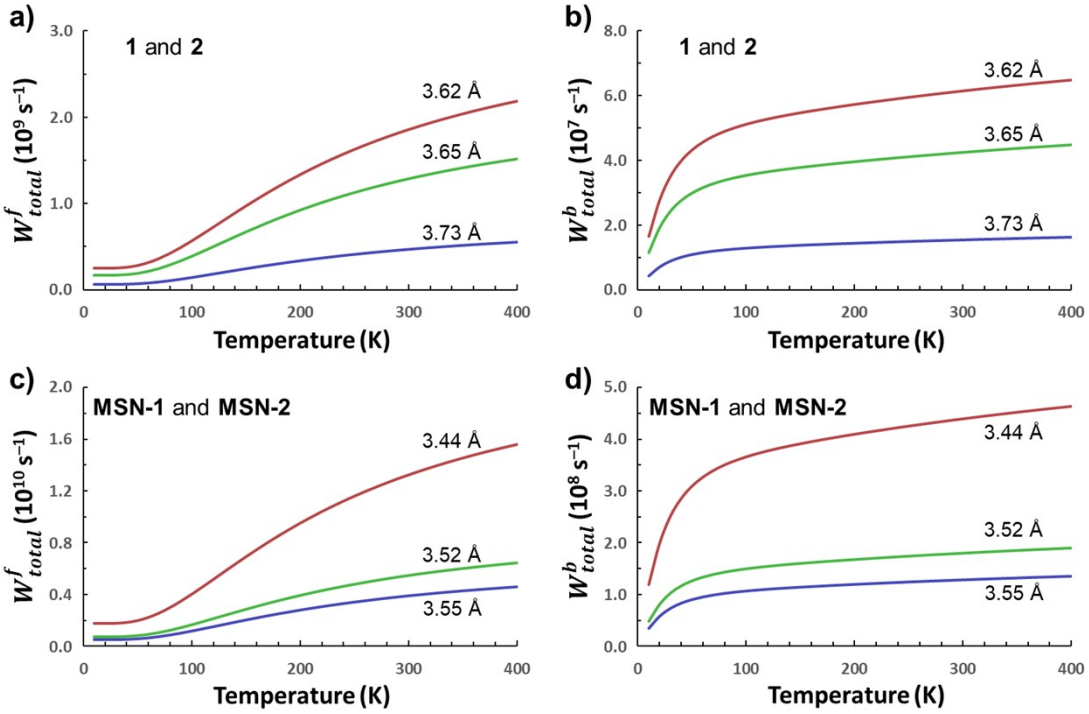

Figure S17. Pairwise energy transfer rates according to Tb–Eu distance for **1**, **2**, **MSN-1**, and **MSN-2**. W^f_{total} and W^b_{total} represent the forward and backward rate, respectively.

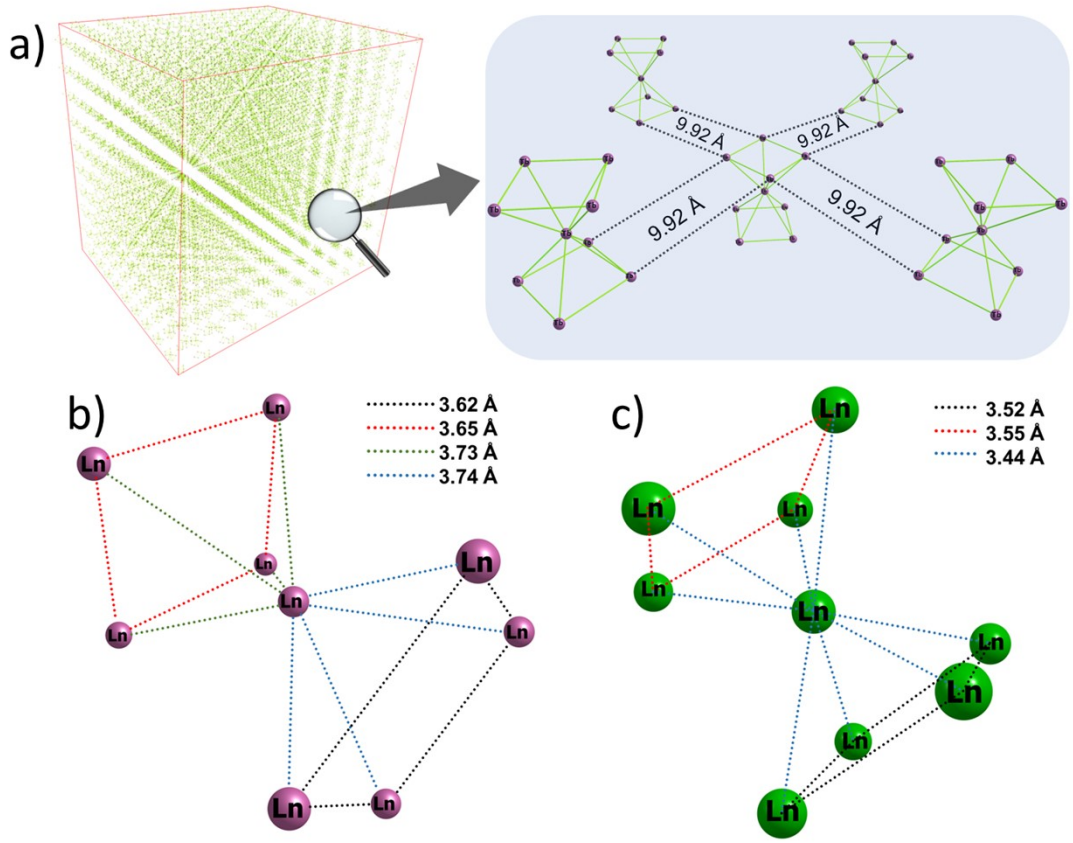

Figure S18. a) View of the 20x20x20 sublattice with a zoom-in, showing the distance between different Ln_9 molecules. The shortest distance between Ln^{3+} ions in two different compounds is 9.92 Å. Interionic distances in a single Ln_9 compound for compounds **1** and **2** (b) and when there are incorporated in **MSN-1** and **MSN-2** nanoparticles (c).

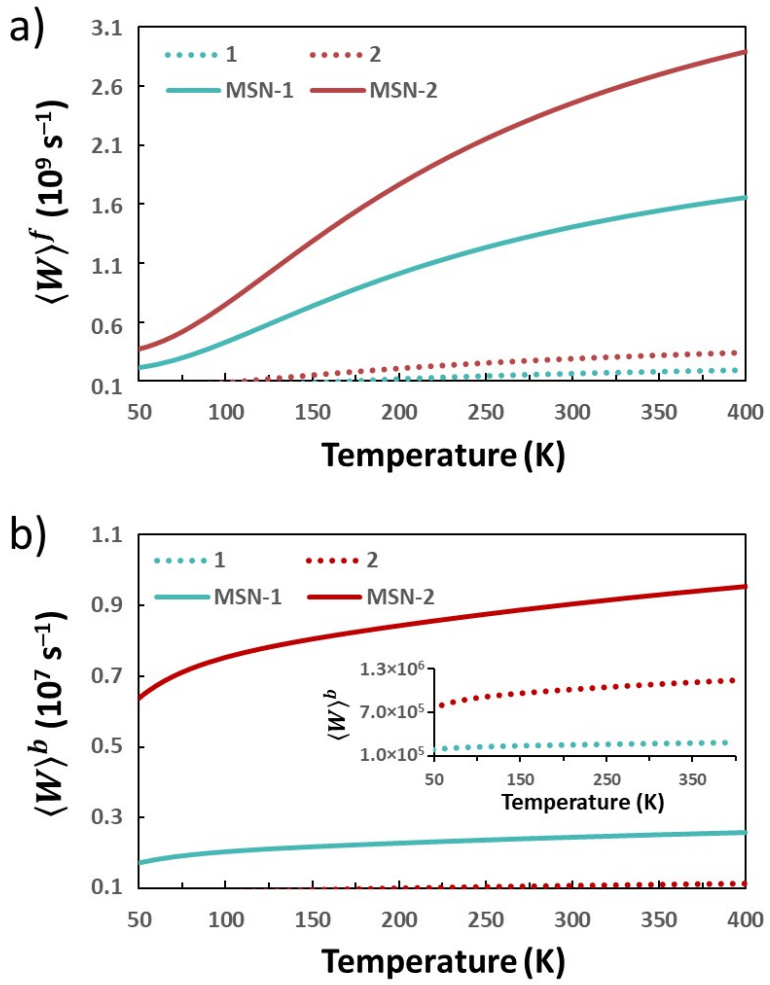

Figure S19. a) Forward (Tb→Eu, $\langle W \rangle^f$) and b) backward (Eu→Tb, $\langle W \rangle^b$) average energy transfer rates for compounds **1**, **2**, and them inside MSN structures.

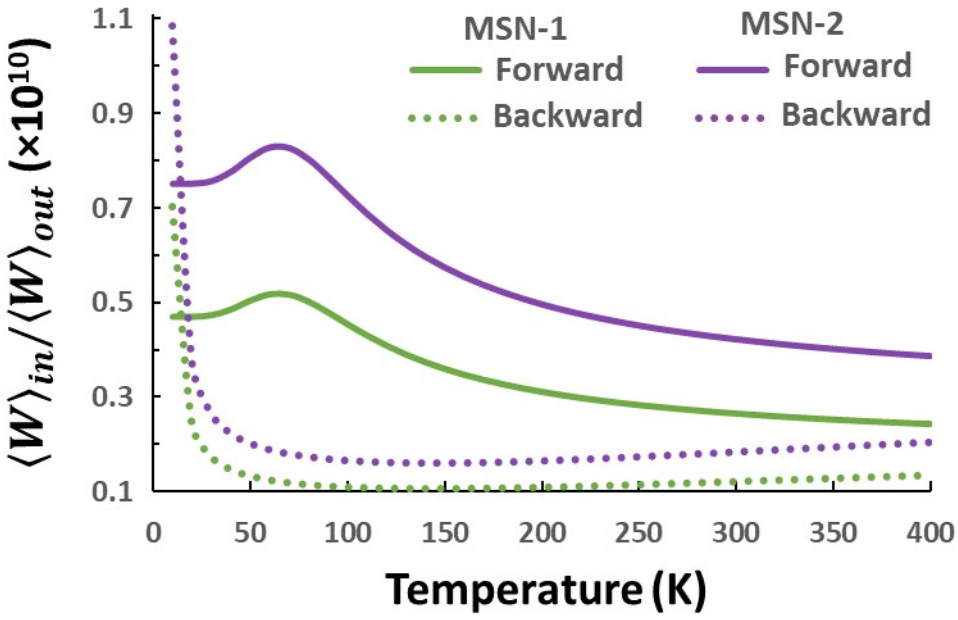

Figure S20. Ratio of energy transfer rates inside ($\langle W \rangle_{in}$) and between two neighboring clusters ($\langle W \rangle_{out}$) as a function of temperature.

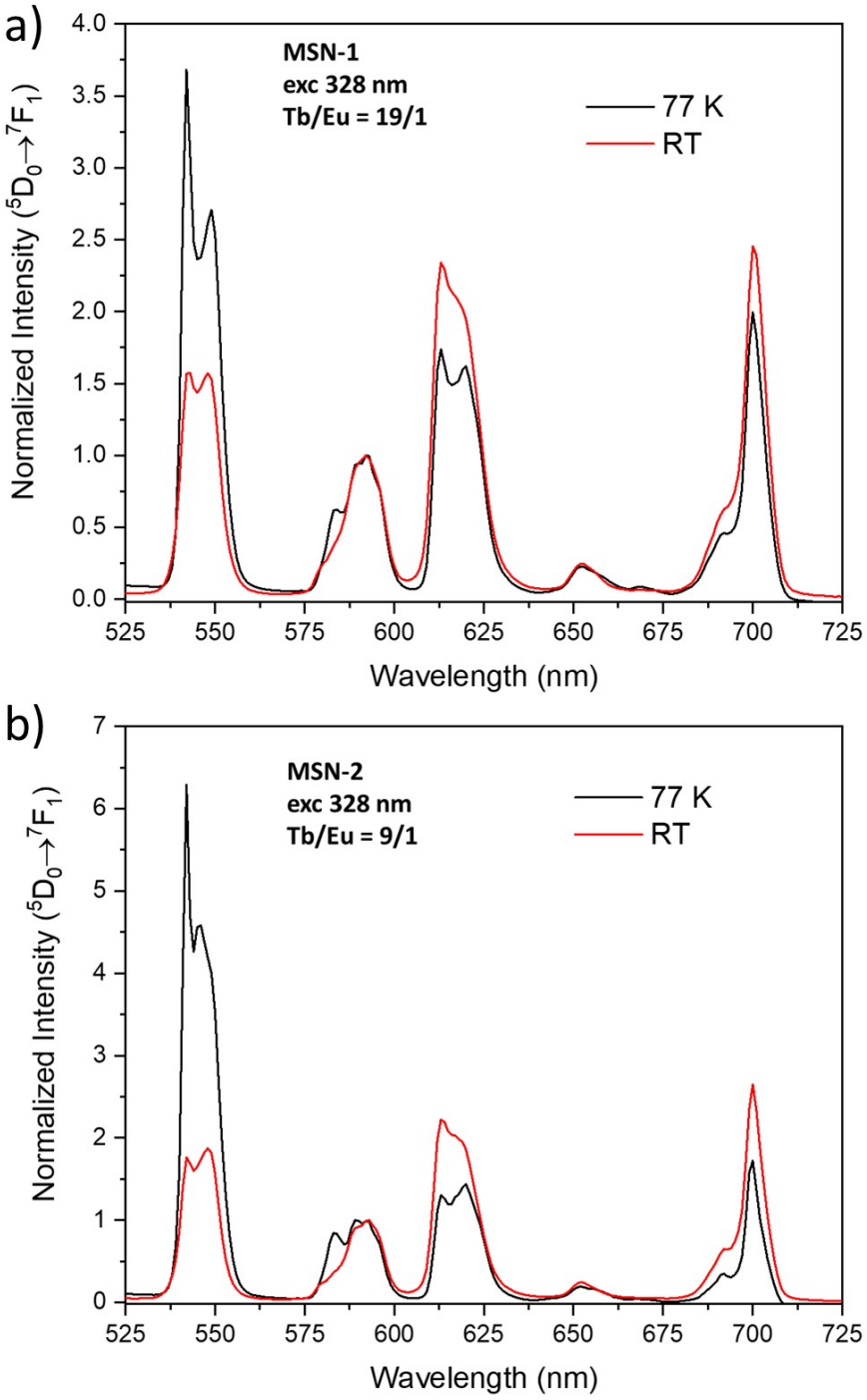

Figure S21. Emission spectra in solid state for: a) **MSN-1** and b) **MSN-2** at 77 K (black lines) and room temperature (red lines).

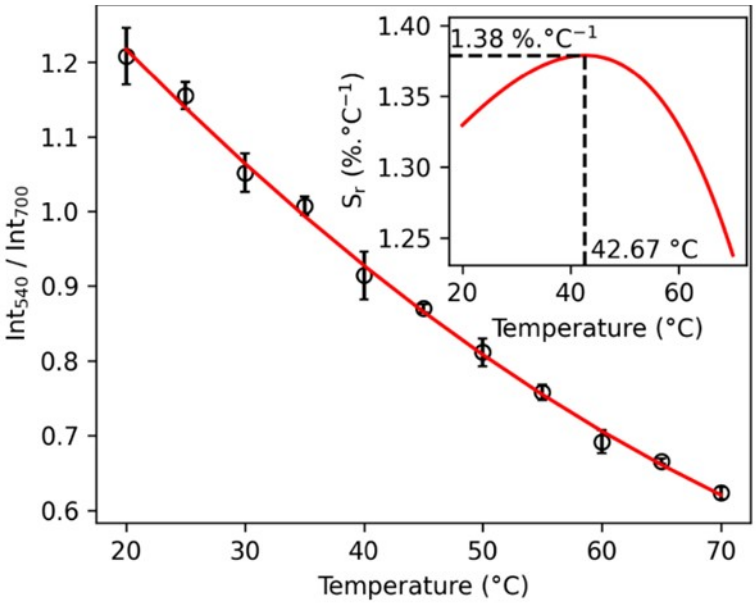

Figure S22. LIR between the $^5D_4 \rightarrow {}^7F_5$ (Tb^{3+}) and $^5D_0 \rightarrow {}^7F_4$ (Eu^{3+}) transitions for thermometry experiments of **MSN-1**. The solid line represents a second-degree polynomial fitting. Integrated areas: 530-560 nm (Tb^{3+}: $^5D_4 \rightarrow {}^7F_5$) and 680─715 nm ($Eu^{3+}$: $^5D_0 \rightarrow {}^7F_4$). Insert: temperature dependence of S_r. The error bars correspond to the standard error of the mean determined from three consecutive temperature cycles.

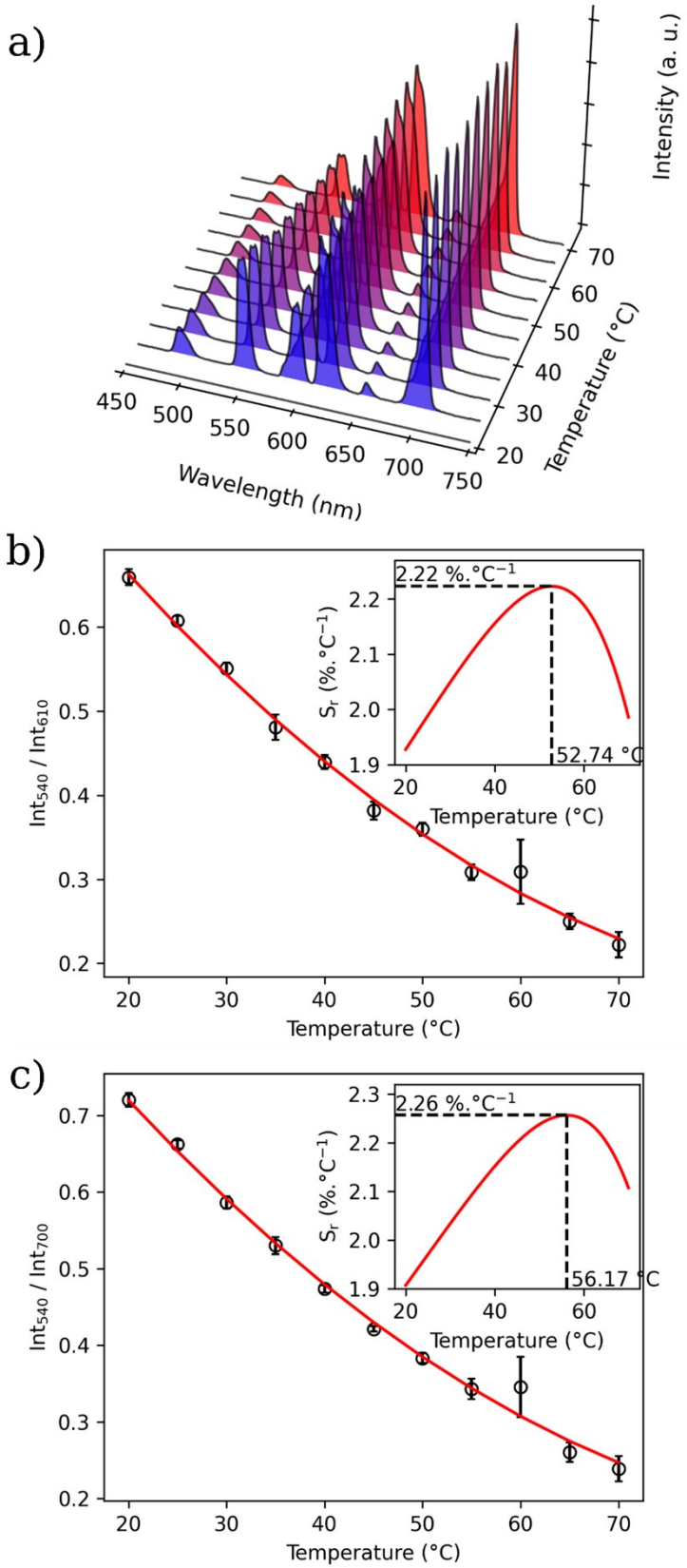

Figure S23. a) Emission spectra (λ_{ex} = 314 nm) of **MSN-2** at every 5 °C from 20 to 70 °C measured in water; and b) corresponding LIR between the emissions at 545 nm and 615 nm; c) corresponding LIR between the emissions at 545 nm and 700 nm. The red line represents a second-degree polynomial fitting. Integrated areas: 530-560 nm (Tb^{3+} $^5D_4 \rightarrow {}^7F_5$) and 604-642 nm ($Eu^{3+}$ $^5D_0 \rightarrow {}^7F_2$) or 680-715 nm ($Eu^{3+}$ $^5D_0 \rightarrow {}^7F_4$). The error bars correspond to standard error of mean determined from three consecutive temperature cycles.

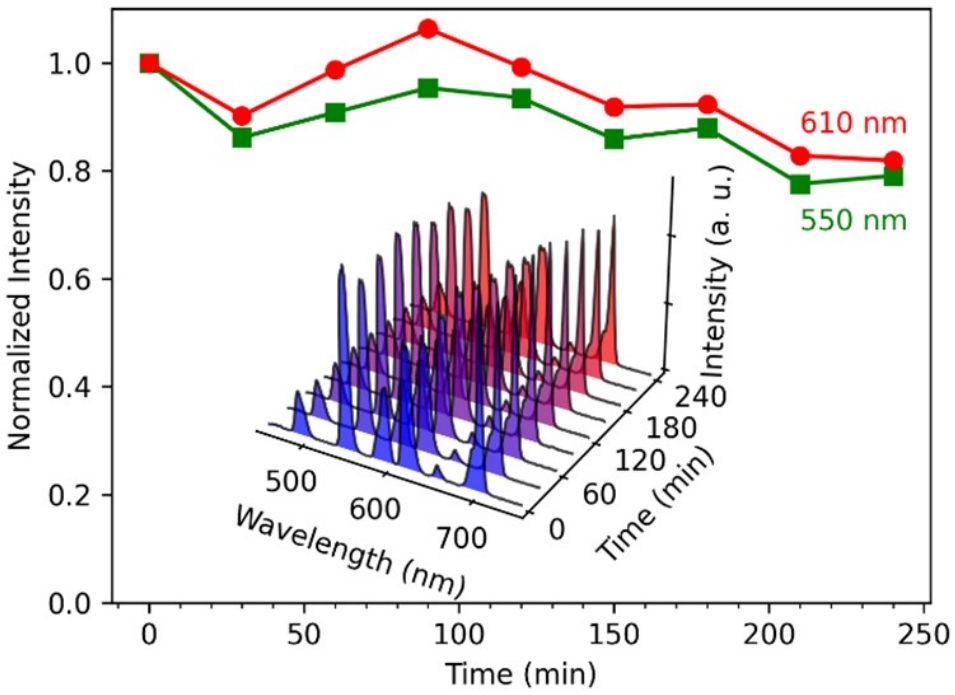

Figure S24. Relative integrated intensities at 550 nm (green) and 610 nm (red) for **MSN-1** in water, normalized to the spectrum measured at time t = 0, after different periods of exposure to continuous excitation light (λ_{ex}=310 nm). Wavelength ranges for integrating areas: 530─560 nm (Tb^{3+}: $^5D_4 \rightarrow {}^7F_5$) and 604─642 nm ($Eu^{3+}$: $^5D_0 \rightarrow {}^7F_2$). Insert: Emission spectra of **MSN-1** after different periods of exposure to excitation light (λ_{ex}=310nm) from 0 to 4 hours.

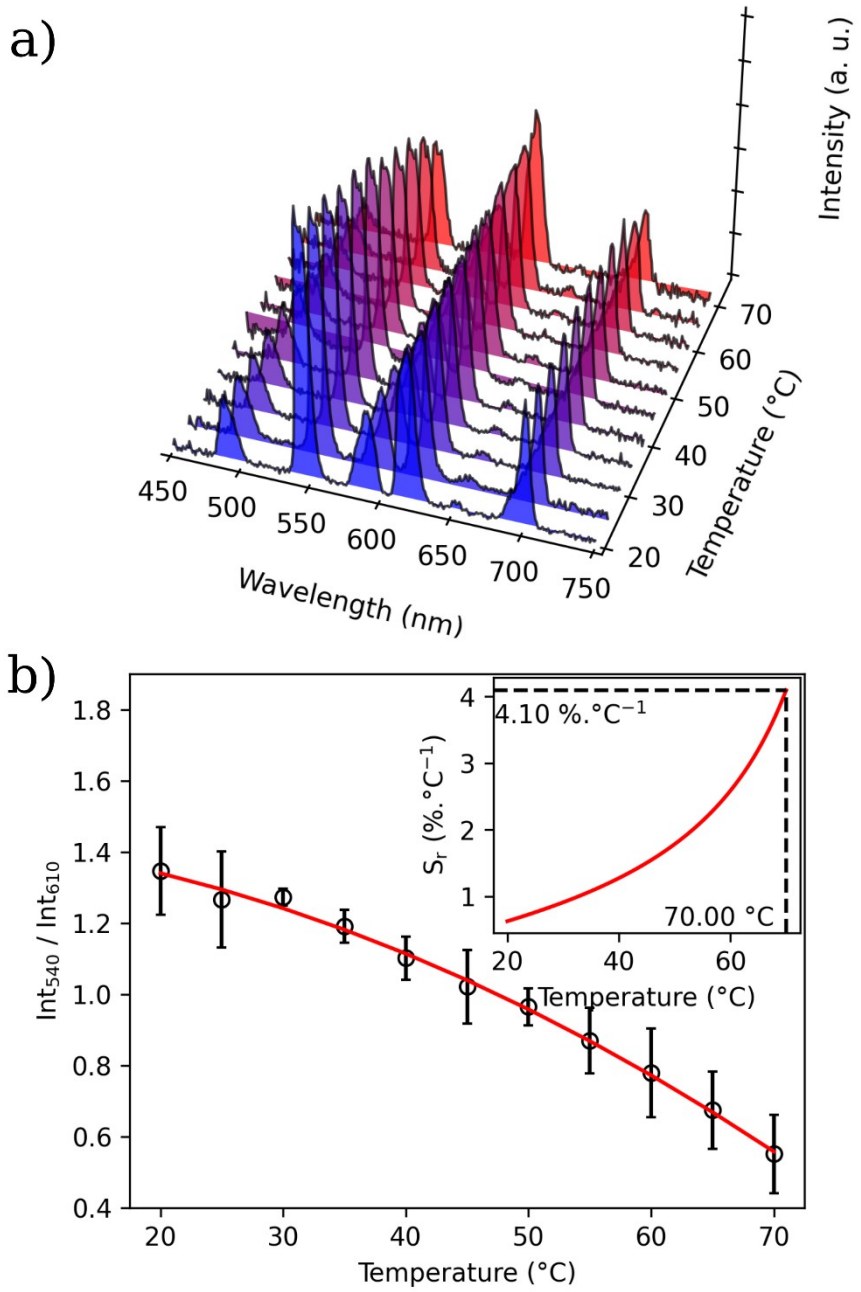

Figure S25. a) Emission spectra (λ_{ex} = 310 nm) of MSN-1 at every 5 °C from 20 to 70 °C measured in PBS; and b) corresponding LIR between the emissions at 540 nm and 610 nm; c) corresponding LIR between the emissions at 545 nm and 700 nm. The red line represents a second-degree polynomial fitting. Integrated areas: 530-560 nm (Tb^{3+} $^5D_4 \rightarrow {}^7F_5$) and 604-642 nm ($Eu^{3+}$ $^5D_0 \rightarrow {}^7F_2$). The error bars correspond to standard error of mean determined from three consecutive temperature cycles.

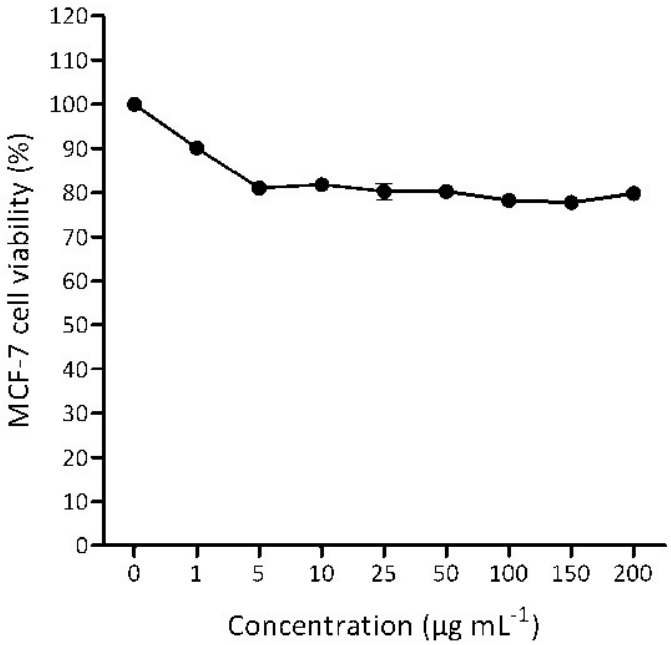

Figure S26. Toxicity effect of MSN-1 on human breast cancer (MCF-7) cell line after 3 days of treatment with several concentrations from 0 to 200 $\mu g \cdot mL^{-1}$. Results are presented as mean ± standard error of the mean (SEM), (n=8).

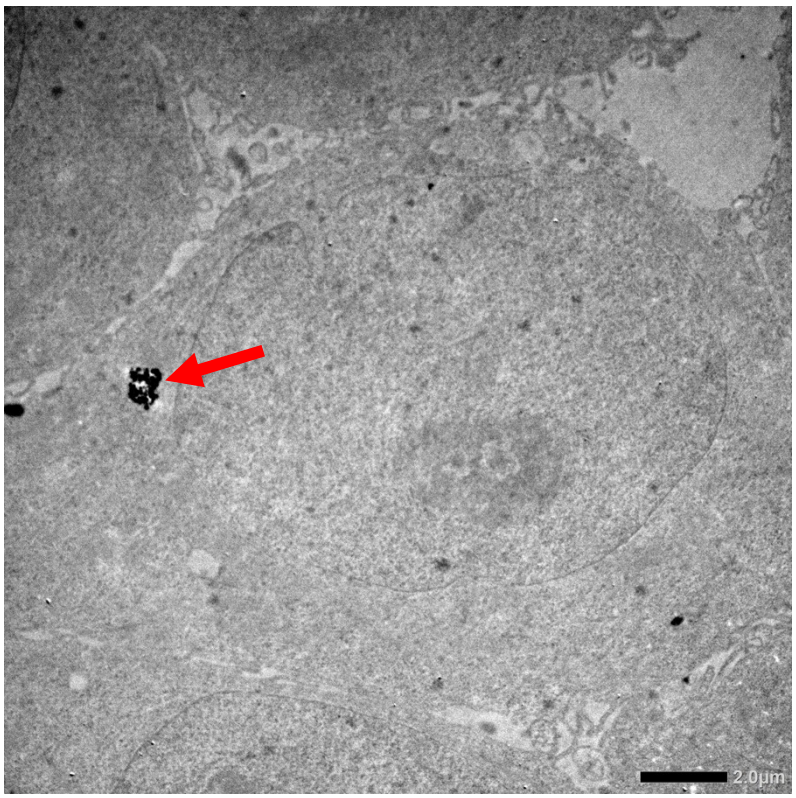

Figure S27. TEM image demonstrating the integration of MSN-1 nanoparticles inside the MCF-7 living cells after 24h of incubation with 100 $mg \cdot mL^{-1}$ of nanoparticles. Arrow indicates the position of nanoparticles.

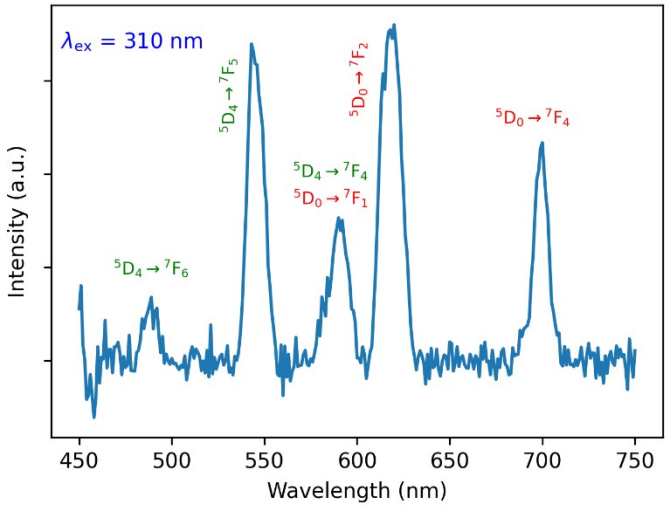

Figure S28. Emission spectrum of the suspension of Y-29 cell line treated with 100 μg·mL^{-1} of MSN-1 for 24 h in PBS performed with λ_{ex} = 310 nm at room temperature.

2. Theoretical calculations

2.1. Structural and Judd-Ofelt analysis

There are nine positions in which the Ln^{3+} can occupy (Figure 4a) for each $[(Tb/Eu)_9(acac)_{16}(\mu_3\text{-}OH)_8(\mu_4\text{-}O)(\mu_4\text{-}OH)\cdot H_2O$ unit, the central site is a perfect C_4 group (deviation R = 0.00, coordination number = 8) while the adjacent positions (Figure 4b) are close to a nonaxial C_s group (R = 0.11, coordination number = 7). However, when the $[(Tb/Eu)_9(acac)_{16}(m_3\text{-}OH)_8(m_4\text{-}O)(m_4\text{-}OH)]\cdot H_2O$ (**1** and **2** when the Tb/Eu ratio is 19/1 and 9/1, respectively) is incorporated in the mesostructured silica nanoparticles (MSN), the complex may undergo a slight structural change (Figure 4), and this leads in the difference in the emission spectra of the pristine compounds (**1** and **2**) and their corresponding **MSN-1** and **MSN-2** nanostructured materials. Therefore, the inclusion of the complexes inside the MSN could approximate the adjacent sites to the central one, leading to a new coordination mode with the central oxygen atoms in situated in the C_4 axis, changing their coordination number from 7 to 8 and, therefore, their point group symmetry from C_s to C_{4v} (Figure 4). This explains the changing of the intensities of $^5D_0 \rightarrow {}^7F_2$ and $^5D_0 \rightarrow {}^7F_4$ emissions once the complexes in **MSN-1** and **MSN-2** present only Ln^{3+} sites with C_4 axes, leading to relatively high intensity of the $^5D_0 \rightarrow {}^7F_4$ and low intensity of $^5D_0 \rightarrow {}^7F_2$ (taking the $^5D_0 \rightarrow {}^7F_1$ as a reference), as discussed by Kariaka *et al.*[1]

The analysis above directly reflects the values of the so-called Judd-Ofelt intensity parameters Ω_λ ($\lambda = 2, 4, 6$). The Eu^{3+} ion is known as a good spectroscopic probe to assess the chemical environment around it due to its magnetic dipole allowed $^5D_0 \rightarrow {}^7F_1$ and the fact that the $^5D_0 \rightarrow {}^7F_\lambda$ ($\lambda = 2, 4, 6$) depend only on their respective reduced matrix elements $\langle {}^7F_\lambda \| U^{(\lambda)} \| {}^5D_0 \rangle$.[2,3] Thus, from the emission spectra of the Eu^{3+}, we can obtain the values of Ω_λ taking as a reference the $^5D_0 \rightarrow {}^7F_1$ transition:

$$\Omega_\lambda = \frac{3\hbar c^3 A_{0\rightarrow\lambda}}{4e^2\omega^3\chi\langle {}^7F_\lambda \| U^{(\lambda)} \| {}^5D_0 \rangle^2} \quad \text{(S1)}$$

where $\chi = n(n^2+2)^2/9$ is the Lorentz local field correction and n is the linear index of refraction of the medium ($n \approx 1.5$ for most cases of Eu-based β-diketonate complexes [2]). ω is the angular frequency of the incident radiation field. The values of the squared reduced matrix elements $\langle {}^7F_\lambda \| U^{(\lambda)} \| {}^5D_0 \rangle^2$ are equal to 0.0032 and 0.0023 for $\lambda = 2$ and 4,[3] respectively. Since the $^5D_0 \rightarrow {}^7F_6$ is very weak and rarely observed, this transition will not be addressed here.

The spontaneous emission coefficients $A_{0\rightarrow\lambda}$ can be calculated by:

$$A_{0\rightarrow\lambda} = A_{0\rightarrow1}\left(\frac{S_{0\rightarrow\lambda}}{S_{0\rightarrow1}}\right) \quad with \quad A_{0\rightarrow1} = \frac{e^2\omega^3\hbar}{3mc^5}n^3\langle {}^7F_1 \| L + 2S \| {}^5D_0 \rangle^2 \tag{S2}$$

The quantity $A_{0\rightarrow1}$ can be used as an internal reference and corresponds to the spontaneous emission coefficient for the transition allowed by magnetic dipole $^5D_0 \rightarrow {}^7F_1$. The square of the reduced matrix element $\langle {}^7F_1 \| L + 2S \| {}^5D_0 \rangle^2 = 0.116$ can be estimated using free-ion wavefunctions in the intermediate coupling scheme,[4] leading to $A_{0\rightarrow1} \cong 50$ s^{-1} for $n = 1.5$. The values $S_{0\rightarrow\lambda}$ are the areas under the emission curves $^5D_0 \rightarrow {}^7F_\lambda$ ($\lambda = 2$ and 4). It is worth mentioning that Eqs. (S1) and (S2) are valid only for Eu^{3+}-based compounds.

Given the presence and the number of peaks of certain Eu^{3+} transitions when the compound **1** is excited at 465 nm (Eu^{3+} $^7F_0 \rightarrow {}^5D_2$), the emission spectra in Figures S13d and S14d confirm that the majority of Eu^{3+} is close to a C_s point group symmetry.[5] Note that the Judd-Ofelt intensity parameters for Eu^{3+} in compounds **1** and **2** should be almost equal once their difference consists only in the stoichiometry of Tb^{3+} and Eu^{3+} ions.

The obtained values of Ω_λ (Table S2) show an uncommon trend of $\Omega_4 > \Omega_2$ for the cases of **MSN-1** and **MSN-2** materials. This indicates that the Eu^{3+} ion occupies a center close to a distorted cube (*e.g.* C_{4v}),[1,6–8] in accordance with the distorted structure when the complexes are incorporated into the MSN structure (Figure 4c), changing the coordination number of the adjacent Ln^{3+} sites from 7 (Figure 4b) to 8 (Figure 4c). Figure 4f shows the structures side-by-side and it can be noted that these structures differ slightly.

From the experimental values of Ω_2 and Ω_4 we can estimate, by a fitting procedure in the JOYSpectra web platform,[9] the physical-chemistry environment parameters such as ligating atom polarizabilities (α') and charge factor (g).[10,11] To obtain those parameters, a simple procedure is done for compound **1** in the JOYSpectra:

i) Substituing 8 Ln^{3+} sites for Y^{3+} and keeping one site with the Eu^{3+};

ii) Inserting the values of Ω_2 and Ω_4 (Table S2);

iii) Marking the checkbox to do a fitting procedure;

iv) Filling the fields “Dynamic Coupling” and “Forced Electric Dipole” mechanisms with “FIT1” or “FIT2” for each type of ligand (*e.g.*, FIT1 for oxygen atoms pertain to HO^- and FIT2 to oxygen from acac ligand) and start the calculation;

v) Using the same values obtained for α' and g and calculate, without the fitting procedure, the Ω_λ with Tb^{3+} intead of Eu^{3+} ion.

The above procedure is a good approximation to obtain the Tb^{3+} Ω_λ parameters theoretically because polarizabilities α' and charge factors g are more related to the ligand’s electronic nature that remains the same.[11]

Table S2 shows the set of Ω_λ for **1** attributed to the Tb^{3+} ion. With this set of Ω_λ, we can conclude that the peak attributed to Tb^{3+} $^5D_4 \rightarrow {}^7F_4$ and Eu^{3+} $^5D_0 \rightarrow {}^7F_1$ transitions in Figure 3b has a more predominance of the Eu^{3+} transition for two main reasons: i) the radiative component of Eu^{3+} $^5D_0 \rightarrow {}^7F_1$ is around 50 s^{-1} while the Tb^{3+} $^5D_4 \rightarrow {}^7F_4$ is approximately 24 s^{-1}; ii) the population of Eu^{3+} $^5D_0$ is higher than the Tb^{3+} $^5D_4$ due to the $Tb^{3+} \rightarrow Eu^{3+}$ energy transfer. The last point will be detailed in the next section.

2.2. Pairwise Tb-to-Eu energy transfer

The energy transfer rates between Tb^{3+} and Eu^{3+} ions were calculated considering the dipole-dipole (W_{d-d}), dipole-quadrupole (W_{d-q}), quadrupole-quadrupole (W_{q-q}), exchange (W_{ex}), [12,13] and magnetic dipole-magnetic dipole (W_{md-md}) mechanisms:[14,15]

$$W_{d-d} = \frac{(1-\sigma_1^D)^2(1-\sigma_1^A)^2\, 4\pi e^4}{(2J_D^*+1)(2J_A+1)3\hbar R^6}\left(\sum_\lambda \Omega_\lambda^D \langle \psi_D J_D \| U^{(\lambda)} \right. \quad \text{(S3)}$$

$$W_{d-q} = \frac{(1-\sigma_1^{D,A})^2(1-\sigma_2^{A,D})^2 \pi e^4}{(2J_D^*+1)(2J_A+1)\,\hbar R^8}\langle f \| C^{(2)} \| f \rangle^2 \times \left[\left(\quad \text{(S4)}$$

$$W_{q-q} = \frac{(1-\sigma_2^D)^2(1-\sigma_2^A)^2\, 28\pi\, e^4}{(2J_D^*+1)(2J_A+1)\,5\hbar\, R^{10}} \times \langle r^2 \rangle_D^2 \langle r^2 \rangle_A^2 \langle f \| \quad \text{(S5)}$$

$$W_{ex} = \frac{2\pi}{\hbar}\left[\left(\frac{e^2}{R}\right)\rho_{f-f}^{\;2}\right]^2 F \quad \text{(S6)}$$

$$W_{md-md} = \frac{(1-\sigma_1^D)^2(1-\sigma_1^A)^2\, 4\pi \mu_B^{\;4}}{(2J_D^*+1)(2J_A+1)3\hbar\, R^6}\langle \psi_D J_D \| L + 2S \| \psi_D^* J_D^* \rangle^2 \times \langle \psi_A^* J_A^* \| L + 2S \| \psi \quad \text{(S7)}$$

where Ω_λ are the intensity parameters considering on the FED mechanism contribution (values in parentheses in Table S2) due to opposite parity configuration mixing (odd-ranking of the ligand field).[11,12,16] The indexes A and D mean acceptor and donor, respectively.

In Eq. S6, ρ_{f-f} is the overlap integral between the 4*f* subshells of the donor and acceptor lanthanide ions.[17] The ρ_{f-f} decays very fast to zero with the increase of R (donor–acceptor distance)[17] and this is the reason why the rate W_{ex} could be neglected in systems with high values of donor-acceptor distances. In the present case, the shortest distances between Tb^{3+} and Eu^{3+} are R = 3.62, 3.65, 3.73 and 3.74 Å (Figure S17) for compounds **1** and **2**, leading to very high values of ρ_{f-f} (4.32×10^{-3} , 3.98×10^{-3}, 3.18×10^{-3}, and 3.10×10^{-3}, respectively) and the exchange mechanism is effective in the energy transfer process.[12] In the case of **MSN-1** and **MSN-2**, the confinement of the complexes provided a shortening of these distances (R = 3.52, 3.55, 3.44 and 3.44 Å, respectively), leading to even higher values of ρ_{f-f} (5.65×10^{-3} , 5.22×10^{-3}, 6.98×10^{-3}, and 6.98×10^{-3}, respectively), which may improve the Tb–Eu energy transfer efficiency.

In Eq. S7, $\mu_B\left(=\frac{e\hbar}{2m_e c}\right)$ is the Bohr magneton and the matrix elements $\langle \psi J \| L + 2S \| \psi^* J^* \rangle$ were estimated using the intermediate coupling scheme with Ofelt's eigenfunctions.[4,14,15] The shielding factors $(1-\sigma_k)$ for donor and acceptor (with $k = 1$ and 2) are given by:[18]

$$\left(1-\sigma_k^{D,A}\right) = \rho(2\beta)^{k+1} \quad \text{(S8)}$$

where ρ is the overlap integral between the valence subshells of the ligating atom and the 4*f* subshell of the lanthanide ion in the case of Eu–O chemical bonds while $\beta = 1/(1 \pm \rho)$ defines the centroid of the electronic density of Eu–O.

For the case of Ln^{3+}-to-Ln^{3+} energy transfer, the spectral overlap factor *F* is calculated using the following analytical expression:[12]

$$F = \frac{ln(2)\ G(\delta,T)}{\sqrt{\pi}\ \ \hbar^2\gamma_D\gamma_A}\left\{\left[\left(\frac{1}{\hbar\gamma_D}\right)^2 + \left(\frac{1}{\hbar\gamma_A}\right)^2\right]ln(2)\right\}^{-\frac{1}{2}} \times exp\left[\frac{1}{4}\frac{\left(\frac{2\delta}{(\hbar\gamma_D)^2}ln2\right)^2}{\left[\left(\frac{1}{\hbar\gamma_A}\right)^2 + \left(\frac{1}{\hbar\gamma_D}\right)^2\right]ln2} - \left(\frac{\delta}{\hbar\gamma_D}\right)^2 ln\right] \quad \text{(S9)}$$

$$with \quad G(\delta,T)\begin{cases} 1 & if\ \ \delta \geq 0 \\ e^{\left(\frac{\delta}{k_B T}\right)} & if\ \ \delta < 0 \end{cases}$$

where $\hbar\gamma_D$ and $\hbar\gamma_A$ are to the bandwidths at half-height (in erg) of the donor and acceptor, respectively. δ is the energy difference between donor and acceptor transitions, $\delta = E_D - E_A$. The temperature dependence is given by the $G(\delta,T)$, which a Boltzmann energy barrier $\exp(\delta/k_BT)$ is activated when $\delta < 0$, where T is the temperature and k_B is the Boltzmann's constant. The calculated forward (Tb^{3+} to Eu^{3+}) and backward (Eu^{3+} to Tb^{3+}) energy transfer rates are presented in Tables S3 and S4, respectively.

2.3. Distribution of Tb–Eu pairs and the average energy transfer rate

Once we calculate the pairwise Tb^{3+}–Eu^{3+} ET rates (Figure S17), we can simulate a Monte-Carlo type distribution of the Tb^{3+} and Eu^{3+} ions in the host matrix using a homemade program written in C language (which can be provided upon request). From the crystallographic data of **1**, we expanded the unit cell (1×1×1) to a larger one (20×20×20, Figure S18a) with a volume of ≈ 44105 nm^3, containing 144000 Tb^{3+} host sites that can be randomly replaced by Eu^{3+} until reaching the desired dopant concentration (in %). We can then obtain the occurrence of Tb–Eu pairs as a function of distance R and concentration $1-x$ of Tb^{3+} throughout the matrix, and consequently, the average forward $\langle W\rangle^f$ and backward $\langle W\rangle^b$ energy transfer rates [14,19] (Eqs. S10 and S11).

$$\langle W\rangle^f = \sum_i \langle W\rangle_i^f = (1-x)\cdot x\left(\sum_i O_i(x) W_i^f\right) \tag{S10}$$

$$\langle W\rangle^b = \sum_i \langle W\rangle_i^b = (1-x)\cdot x\left(\sum_i O_i(1-x) W_i^b\right) \tag{S11}$$

where W_i^f and W_i^b represent the pairwise forward and backward energy transfer rates for the i^{th} Tb–Eu distance (Figure S17) at a given temperature, respectively. The acceptor Eu^{3+} and donor/host Tb^{3+} stoichiometric fractions are represented by x and $1-x$, respectively. The occurrence coefficients O_i are related to the formation of a Tb–Eu pair at distance R_i with respect to the acceptor (for forward energy transfer $\langle W\rangle^f$) or donor (for backward energy transfer $\langle W\rangle^b$) obtained from Monte-Carlo simulations for each Eu^{3+} amount (Eq. S12):[14,19]

$$O_i(1-x) = \frac{N(i)}{s\cdot(1-x)} \quad , \; O_i(x) = \frac{N(i)}{s\cdot x} \tag{S12}$$

where $N(i)$ is the count of Tb–Eu pairs at distance $R(i)$, and s is the number of host sites in the undoped matrix (which equals 144000 host sites in the 20×20×20 expanded cell, Figure S18a). As the backward energy transfer is the energy coming from Eu^{3+} to Tb^{3+}, the "acceptor" in this case is the Tb^{3+}, justifying the use of coefficients $O_i(x)$ instead of $O_i(1-x)$ to calculate $\langle W\rangle^b$. We present all values of $O_i(x)$ obtained from simulations in Table S5 while the $\langle W\rangle^f$ and $\langle W\rangle^b$ rates are in Figure S19.

References

1 N. S. Kariaka, V. A. Trush, V. V. Dyakonenko, S. V. Shishkina, S. S. Smola, N. V. Rusakova, T. Y. Sliva, P. Gawryszewska, A. N. Carneiro Neto, O. L. Malta and V. M. Amirkhanov, *ChemPhysChem*, , DOI:10.1002/cphc.202200129.

2 H. F. Brito, O. M. L. Malta, M. C. F. C. Felinto and E. E. S. Teotonio, in *PATAI'S Chemistry of Functional Groups*, John Wiley & Sons, Ltd, Chichester, UK, 2010.

3 W. T. Carnall, H. Crosswhite and H. M. Crosswhite, *Energy level structure and transition probabilities in the spectra of the trivalent lanthanides in LaF_3*, Argonne, IL, United States, 1978.

4 G. S. Ofelt, *J. Chem. Phys.*, 1963, **38**, 2171–2180.

5 P. A. Tanner, in *Lanthanide Luminescence. Springer Series on Fluorescence (Methods and Applications), vol 7*, eds. P. Hänninen and H. Härmä, Springer-Verlag, Berlin, Heidelberg, 2010, pp. 183–233.

6 M. Bettinelli, A. Speghini, F. Piccinelli, A. N. C. Neto and O. L. Malta, *J. Lumin.*, 2011, **131**, 1026–1028.

7 R. A. Sá Ferreira, S. S. Nobre, C. M. Granadeiro, H. I. S. Nogueira, L. D. Carlos and O. L. Malta, *J. Lumin.*, 2006, **121**, 561–567.

8 A. N. Carneiro, E. Huskowska, P. Gawryszewska, J. Legendziewicz and O. L. Malta, *J. Lumin.*, 2016, **169**, 454–457.

9 R. T. Moura Jr., A. N. Carneiro Neto, E. C. Aguiar, C. V. Santos-Jr., E. M. de Lima, W. M. Faustino, E. E. S. Teotonio, H. F. Brito, M. C. F. C. Felinto, R. A. S. Ferreira, L. D. Carlos, R. L. Longo and O. L. Malta, *Opt. Mater. X*, 2021, **11**, 100080.

10 R. T. Moura Jr., A. N. Carneiro Neto, R. L. Longo and O. L. Malta, *J. Lumin.*, 2016, **170**, 420–430.

11 A. N. Carneiro Neto, E. E. S. Teotonio, G. F. de Sá, H. F. Brito, J. Legendziewicz, L. D. Carlos, M. C. F. C. Felinto, P. Gawryszewska, R. T. Moura Jr., R. L. Longo, W. M. Faustino and O. L. Malta, in *Handbook on the Physics and Chemistry of Rare Earths, volume 56*, eds. J.-C. G. Bünzli and V. K. Pecharsky, Elsevier, 2019, pp. 55–162.

12 O. L. Malta, *J. Non. Cryst. Solids*, 2008, **354**, 4770–4776.

13 A. N. Carneiro Neto, R. T. Moura and O. L. Malta, *J. Lumin.*, 2019, **210**, 342–347.

14 V. Trannoy, A. N. Carneiro Neto, C. D. S. Brites, L. D. Carlos and H. Serier-Brault, *Adv. Opt. Mater.*, 2021, **9**, 2001938.

15 A. N. Carneiro Neto, R. T. Moura, A. Shyichuk, V. Paterlini, F. Piccinelli, M. Bettinelli and O. L. Malta, *J. Phys. Chem. C*, 2020, **124**, 10105–10116.

16 T. Kushida, *J. Phys. Soc. Japan*, 1973, **34**, 1318–1326.

17 A. N. Carneiro Neto and R. T. Moura Jr., *Chem. Phys. Lett.*, 2020, **757**, 137884.

18 O. L. Malta, H. F. Brito, J. F. S. Menezes, F. R. G. e Silva, S. Alves, F. S. Farias and A. V. M. de Andrade, *J. Lumin.*, 1997, **75**, 255–268.

19 X. Qin, A. N. Carneiro Neto, R. L. Longo, Y. Wu, O. L. Malta and X. Liu, *J. Phys. Chem. Lett.*, 2021, **12**, 1520–1541.